



POLITECNICO
MILANO 1863

SCUOLA DI INGEGNERIA INDUSTRIALE
E DELL'INFORMAZIONE

From The Frequency Response of Wooden Plates to their Material Parameters

Tesi di Laurea Magistrale in
Music and Acoustic Engineering

Author: **David Giuseppe Badiane**

Student ID: 943500

Advisor: Prof. Fabio Antonacci

Co-advisors: Sebastian Gonzalez, Raffaele Malvermi

Academic Year: 2020-21

Abstract

Non-destructive wood characterization is an important topic in musical acoustics. Indeed, on one hand the acoustical performance of stringed instruments is tightly linked to the elastic properties of their material. On the other hand, the tonewood employed for building the soundboard (i.e. usually plates of spruce or cedar) displays a high variability in elastic properties. Thus, the first crucial step in instrument making is the choice of the wood. Non-Destructive Testing (NDT) techniques for a fast and accurate characterization of wood would help luthiers in their selection of wood and allow them to make informed design choices on the instrument.

A popular class of NDT techniques are Finite Element Model Updating (FEMU) methods. Usually, these methods involve an experimental campaign performed on the body under study and a finite element model of its vibration. The material parameters are identified by minimizing the difference between the experimentally determined quantity and its numerical counterpart. However, FEMU techniques are not suited to be employed by instrument makers, as they are time consuming and technically challenging.

In order to tackle these problems, in this thesis we present a novel and efficient neural network based technique for the characterization of wooden thin plates. This technique goes by the name of *FRF2Params* and allows to simultaneously estimate the material properties from a single Frequency Response Function (FRF) evaluated at prescribed points of the plate. The FRF is obtained in a non-destructive fashion, employing a hammer-accelerometer measurement system. The neural networks are trained on a synthetic dataset (i.e. obtained with numerical simulations) containing the vibrational data of plates with varying dimensions and material properties.

Our results show that the *FRF2Params* method estimates the material properties in a fast and accurate way. This work paves the way to the development a neural networks-driven tool that can help instrument makers in the making of their instruments.

Keywords: material characterization, non-destructive testing, musical acoustics, machine learning, feedforward neural networks

Abstract in lingua italiana

La caratterizzazione del legno con metodi non distruttivi è un argomento importante nell’acustica musicale. Infatti, da un lato la performance acustica degli strumenti a corda è influenzata dalle proprietà elastiche del loro materiale. Dall’altro lato, il legno utilizzato per costruire la loro tavola armonica (i.e. di solito, piatti di abete o di cedro) mostrano proprietà elastiche altamente variabili. Quindi, il primo passo per la costruzione di uno strumento è la scelta del legno. Tecniche di Controllo Non Distruttivo (CND) per una caratterizzazione del legno veloce e accurata aiuterebbero i liutai sia nella selezione del legno che nel futuro design dello strumento.

Una classe popolare di tecniche CND sono i metodi di Finite Element Model Updating (FEMU). Generalmente, questi metodi coinvolgono una campagna di misure sperimentali sul corpo studiato e un modello a elementi finiti della sua vibrazione. Le proprietà del materiale vengono identificate minimizzando la differenza tra la quantità misurata e la sua controparte calcolata numericamente. Tuttavia, queste tecniche non sono appropriate ad essere utilizzate dai liutai, in quanto sono costose in termini di tempo e tecnicamente complesse.

Per risolvere questi problemi, in questa tesi presentiamo una nuova ed efficiente metodologia, denominata *FRF2Params*, basata su reti neurali per caratterizzare piatti di legno. La tecnica consente di stimare simultaneamente i parametri meccanici a partire da una singola Funzione di Risposta in Frequenza (FRF) valutata per punti di misura prestabiliti. La FRF si può ottenere con un sistema di misura non distruttivo, basato su un piccolo martello e un accelerometro. Le reti neurali sono addestrate tramite un dataset sintetico (i.e. ottenuto con simulazioni numeriche) contenente i dati vibrazionali di piatti di dimensione e proprietà elastiche variabili.

I nostri risultati dimostrano che *FRF2Params* è in grado di stimare le proprietà del legno in modo accurato e veloce. Questo lavoro apre la strada allo sviluppo di uno strumento basato su reti neurali che possa aiutare i liutai durante la costruzione dei loro strumenti.

Parole chiave: caratterizzazione dei materiali, controllo non distruttivo, acustica musicale, machine learning, reti neurali feedforward

Contents

Abstract	i
Abstract in lingua italiana	iii
Contents	v
1 Introduction	1
1.1 Outline Of The Thesis	5
2 Background	7
2.1 The Wood as Material	7
2.1.1 Theory on material properties	7
2.1.2 Mechanical properties of wood	10
2.2 Acoustical Properties of Wood	12
2.3 Resonance Wood And Wood Selection	14
2.3.1 Different types of wood	14
2.3.2 Resonance wood	14
2.3.3 Wood selection	15
2.4 Frequency Response Function	16
2.4.1 Features of a Frequency Response Function	16
2.4.2 Measurement of a Frequency Response Function	19
2.4.3 Estimation of a Frequency Response Fuction	19
2.5 Rayleigh damping	21
2.6 Wooden thin plates in free boundary conditions	23
2.7 Non Destructive Evaluation of Wood	25
2.7.1 Caldersmith's formulas for wooden thin plates	25
2.7.2 Experimental/numerical techniques	26
2.8 Concluding Remarks	27

3 Generation and Analysis of the Dataset	29
3.1 The guitar plate	29
3.2 Dataset Generation	30
3.2.1 Geometry modeling and location of the measurement points	31
3.2.2 Sampling of the input parameters and simulations	32
3.3 Analysis of the dataset	34
3.3.1 Modal shapes Labeling	34
3.3.2 Effect of modes shifts	36
3.4 Concluding Remarks	39
4 Prediction of Frequency and Amplitude	41
4.1 Multilayer feedforward neural networks	41
4.2 Choice of the Topology of the Neural Networks	42
4.3 Generalization	45
4.4 Concluding remarks	46
5 FRF2Params Method	47
5.1 Overview of the method	47
5.2 Minimization	48
5.2.1 Computation of the loss function	49
5.2.2 Model updating	52
5.3 Advantages of the method	53
5.4 Concluding Remarks	54
6 Results of the FRF2Params method	55
6.1 Materials	55
6.2 Results and Discussion	57
6.3 Concluding Remarks	60
7 Conclusions And Future Work	61
7.1 Limitations and Future Works	61
7.2 Limitations	61
7.3 Future Works	62
7.4 Conclusions	63
Bibliography	65

List of Figures	71
List of Tables	75
List of Symbols	78
Acknowledgements	81

1 | Introduction

In stringed instrument making, the mechanical properties of the tonewood employed for the construction of the soundboard are generally tightly connected to the acoustical quality of the instrument. This aspect is stressed in [38], which is focused on piano soundboards, and by [22], which analyses the relationship between mechanical parameters of the soundboard and the acoustical features of Spanish guitars. Since the material properties of tonewood display a great variability [8], the first crucial step in instrument making is the choice of the wood.

Makers pick their wood following cost, mechanical, artistic and workability criteria, as indicated by Viala [56]. Those criteria are addressed through the luthier's sensorial experience and expertise [15], which may fail in the selection of the wood with the best acoustical performance [2]. Indeed, despite expressing great interest in scientific research on their working materials, few makers employ measuring tools and/or a scientific approach to select their wood [12].

Nevertheless, throughout the years many different scientific approaches have been developed for wood characterization. In general, material characterization can be achieved with both direct and indirect methods. Direct methods such as tensile tests [7, 52] represent the most reliable measurements of the elastic properties of a body. Unluckily, such methods are not suited for musical acoustics, as they involve the application of an increasing load until the body breaks or undergoes non elastic deformation. As a consequence, in order to preserve the structural integrity of the wood we need to resort to Non-Destructive Testing (NDT) techniques, that involve the identification of the material properties instead of their measurement.

The earliest NDT techniques for wooden thin plates were presented throughout the 80s. In 1984 Caldersmith, McIntyre and Woodhouse introduce a set of equations that relate the material parameters of the plate to its density, its geometry and the frequency of certain modes of vibration, called characteristic modes of the plate [10, 30–32]. We will refer to such equations as Caldermuth's formulas.

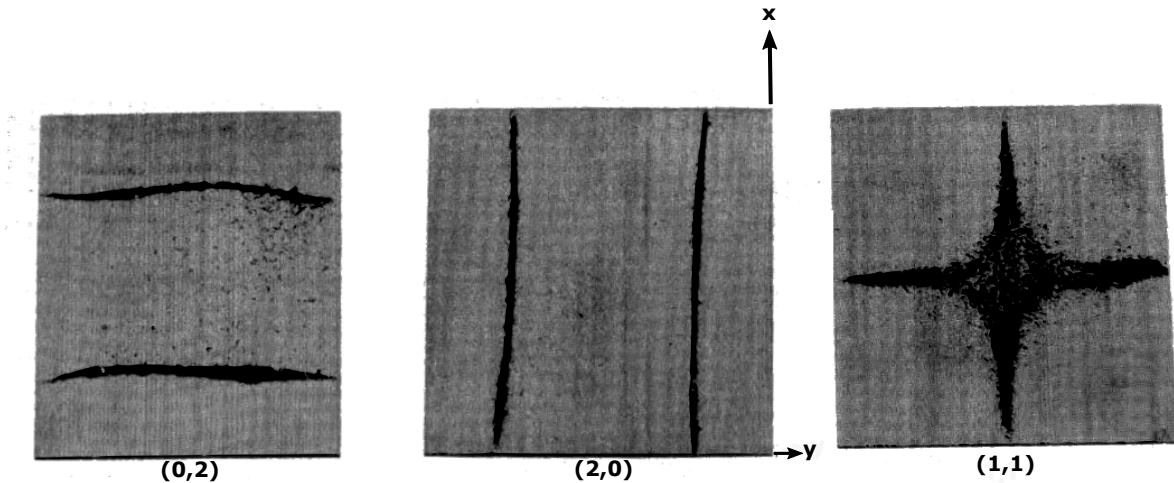


Figure 1.1: Chladni patterns of the modal shapes employed for the estimation of the material parameters of the plate with Caldersmith's formulas (Caldersmith & Freeman, 1990, p. 9 [11])

Experimental procedures exploiting Caldersmith's formulas were defined by Caldersmith himself in 1990 [11] and by Sobue et al. in 1991 [49]. The first demonstrates the feasibility of employing Caldersmith's formulas inside a workshop using Chladni patterns to identify the characteristic modes of the plate, which are shown in Fig. 1.1. Instead, the second one identifies the characteristic modes through an automated algorithm based on the regularity of the resonance frequencies of higher order vibrations. The initial data for developing the algorithm were obtained by employing 95 published datasets containing the elastic constants of more than a hundred species of wood [5, 23, 25]. Sobue claims that this method allows to identify the characteristic modes of the plate with a "degree of correct judgement of about 85%".

In parallel, many researchers employed numerical methods such as Finite Element Method (FEM) along with experimental measurements to determine the material parameters of wooden plates, thus introducing the so called experimental/numerical techniques. A first experimental/numerical approach was undertaken in 1984 by Molin [36]. Through the use of a finite element model he demonstrates that the first three modes of the plate (n.b. which were the characteristic modes of the plates he analysed in his study) can be used to estimate the plate material properties. Moreover he investigates the relation between the plate material properties, the plate dimensions and the modal shapes of the characteristic modes.

The enhancement of experimental/numerical approaches was carried out in 1993 by Sol

[50] and in 1997 by Larsson [27]. In both cases, after having experimentally determined the eigenfrequencies of a wooden thin plate, the identification of the material properties is achieved by updating the material parameters of an equivalent finite element model until the relative error between the experimentally determined eigenfrequencies and their numerical counterpart is minimized. This procedure goes by the name of Finite Element Model Updating (FEMU).

In the recent years, FEMU approaches have been increasingly used. In 2017 Zhou presented a comparative study about the impact that different boundary conditions have on the identification of the elastic constants of rectangular wooden panels with a FEMU approach [61]. For each configuration of boundary conditions, the identified material parameters are compared to the measurements coming from a static tensile test. The results of this study indicate that the best performing configuration is a combination of simply supported edges and free edges (i.e. "SFSF" for each edge of the plate, where *S* and *F* denote simply supported and free boundary conditions, respectively).

In 2018 Viala proposes a method called Finite Element Model Updating on 3D Vibratory Field (FEMU-3DVF) [54]. This technique allows to simultaneously estimate the material and damping parameters of arbitrary geometry objects starting from full field vibratory measurements. Through the FEMU-3DVF method, an estimation of the mechanical parameters of composite violin top-plate can be obtained with an error range between 5.9% and 8.5% for the identification of the longitudinal and radial Young moduli E_L , E_R and for the longitudinal to radial shear modulus G_{LR} [55]. An application of FEMU-3DVF method on wooden plates can be found in [56].

Despite overcoming the geometry constrains, the work made in [54] is still not enough to form a self-contained, portable framework that can help luthiers in building musical instruments inside their own workshops for two main reasons. First, FEMU has the inconvenient of being time consuming. Suppose that a single FEM simulation for the computation of the eigenfrequencies takes 18 seconds and that the minimization involves 400 iterations (n.b. both assumptions are optimistic), the time required for a single estimation would be of about 2 hours. Second, the FEMU-3DVF method requires expensive equipment, such an optic vibrometer, which is unaffordable for many instrument makers.

A different approach is undertaken by Mehrez et al., who propose a data-driven method that allows the stochastic characterization of composite materials [33, 34]. The method is based on a dataset containing the experimentally determined vibrational data of 21 beam specimens along with their elastic constants, which are identified with a FEMU approach. The knowledge inferred from the data is then exploited in order to achieve a

satisfactory characterization of the material. The technique resorts to statistical methods such as data augmentation. The main drawback of this approach is that the campaign of experimental measurements is extremely burdensome in terms of time.

The employment of FEM-based datasets, i.e. synthetic datasets, is a good alternative to speed up the time spent for obtaining a dataset. This particular data-driven approach is applied to violin top-plates for the first time by Gonzalez [18]. This work starts from a dataset generated by running thousands of FEM simulations of the parametric violin top-plate mesh presented in [17]. Using classical statistical learning tools, Gonzalez provides highly informative findings for violin making. In particular he investigates the impact that variations of outline, thickness profile and material parameters have on the vibrational response of the violin top. He also shows that the dataset can be used to train a neural network that accurately predicts the eigenfrequencies of a violin top-plate as its outline changes.

In this thesis a similar data-driven approach is undertaken in order to characterize the wood of thin rectangular plates. We present an updating-based procedure called *FRF2Params* method that allows to simultaneously estimate the plate material parameters. The *FRF2Params* requires as inputs a point Frequency Response Function (FRF) evaluated at prescribed points of the plate, the geometry and the density of the plate.

The complete pipeline of the method is shown in Fig. 1.2. The first step is to define the location the excitation and measurement points, measure the FRF of the plate that the user wants to characterize and build an equivalent finite element model. The finite element model is used to generate a synthetic dataset containing the eigenfrequencies of the plate and the corresponding amplitudes in the FRF for plates of varying geometry and material properties. Subsequently, the dataset is employed to train two feedforward neural networks, one for frequency and another one for amplitude. The last step involves the minimization of the relative frequency distance between each peak of the measured FRF and the closest simulated peak provided by the neural networks. The geometry and the density of the plate are fixed during a minimization task. As a result, the minimization runs on the multidimensional space defined by the elastic constants of the plate only. The final estimate of the material properties is obtained by averaging the outputs of an arbitrary number of minimization tasks that differ one another for the value assigned to the density.

The use of neural networks allows to greatly accelerate the computation time without a significant loss of accuracy. The computational effort is shifted to the generation of the dataset, while the estimation process itself is fast and accurate. Given these features, the

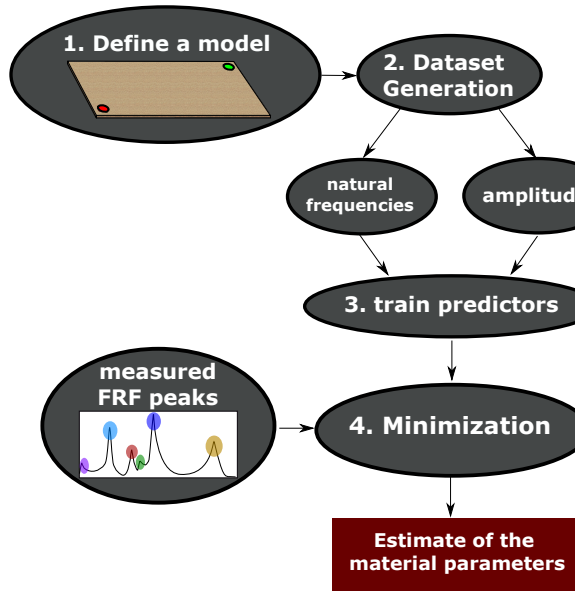


Figure 1.2: Complete pipeline of the *FRF2Params* method.

FRF2Params method can be thought as an enhancement of FEMU methods where the inputs of a neural network are updated instead of a finite element model. As a result, the *FRF2Params* method could define a novel class of non-destructive techniques for material characterization called *neural network updating* methods.

The *FRF2Params* method represents a first step towards an experimental neural network-based procedure that can be employed by instrument makers in their workshops. That is, the required measurement tools (i.e. a dynamometric hammer and an accelerometer) are affordable and no further analysis of the acquired FRF is necessary.

1.1. Outline Of The Thesis

In Chapter 2 the basic concepts that will extensively used in this thesis are introduced. In particular, we first describe the mechanical and the acoustical properties of wood and how instrument makers select their wood. Then, we discuss and define the concepts of frequency response function, vibration of wooden thin plates and Rayleigh damping. At last, we provide an overview of NDT techniques for material characterization in the state of the art.

In Chapter 3 the generation of the dataset that will be used to estimate the material properties of the plate is described in depth. Moreover, the dataset is analysed, focusing on its input/output relation.

In Chapter 4 the neural networks that predict the vibrational data of the plates are introduced and the accuracy of their prediction is discussed.

In Chapter 5 the *FRF2Params* method is illustrated in depth and its advantages are described.

In Chapter 6 the *FRF2Params* method is validated on a set of 10 plates and the results are given and discussed.

In Chapter 7 the features of the *FRF2Params* method are summarized, the limitations of the technique are delineated along with possible future works and improvements.

2 | Background

In this Chapter, the basic concepts that will be extensively used throughout the thesis are presented. First, we illustrate the mechanical and acoustical properties of wood. Secondly, we introduce resonance wood, which is the wood employed for the construction of the soundboards of stringed instruments, and describe how instrument makers select their wood. Subsequently, we discuss the frequency response function and give the basic concepts of eigenfrequency and modal shape. Moreover, we describe in depth the measurement and the acquisition of a frequency response function. Afterwards, we illustrate Rayleigh damping, as it is the damping model that will be employed in this thesis. Next, since this thesis is focused on the characterization of wooden thin plates in free boundary conditions, we describe their vibration focusing on their eigenfrequencies and modal shapes. At last, we provide an overview of the current vibration-based non-destructive testing techniques for the characterization of wood.

2.1. The Wood as Material

2.1.1. Theory on material properties

An anisotropic material is a material whose vibrational response to a specific loading force depends on the direction of the force itself. Such materials can be described by three types of mechanical parameters, namely the modulus of elasticity, the modulus of rigidity and the Poisson ratio.

Consider a Cartesian reference system and denote by $\mathbf{x} = [x_1, x_2, x_3]$ the vector representing the position of a generic point and an element of material undergoing a static point load as in Fig. 2.1. The displacement of the material will also be a vector $\mathbf{u} = [u_1, u_2, u_3]$.

The stress σ_{ij} on the plane normal to the x_i direction due to a force acting on the x_j direction is defined as the ratio of the force F_j to the area A_i of the surface perpendicular

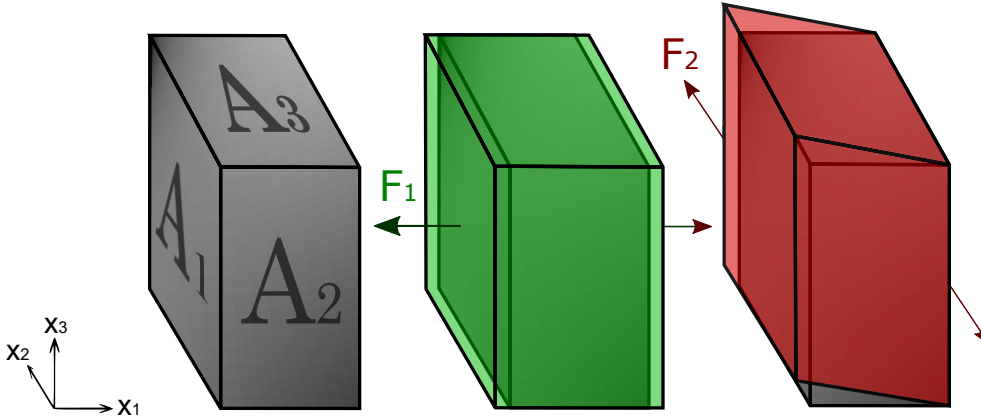


Figure 2.1: Application of an axial load F_1 and a shear load F_2 , considering the surface A_1 . $\sigma_{11} = F_1/A_1$ is the axial stress along the x_1 direction, while $\sigma_{12} = F_2/A_1$ is the shear stress along the x_1 and x_2 directions. When loading the body over the surface A , a reacting force of equal magnitude and opposite verse will appear on the opposite surface due to the third principle of dynamics.

to the x_i direction, namely

$$\sigma_{ij} = \frac{F_j}{A_i}. \quad (2.1)$$

If $j = i$, the stress is axial because the load is perpendicular to the surface where it is applied. On the other side, if $i \neq j$, the stress takes the name of shear or transverse stress, since the load is parallel to the surface where it is applied. An example of axial and shear loads are depicted in Fig. 2.1 in green and red, respectively.

In general, a stress applied on a solid element causes the deformation of the element itself. The deformation of the element along a given plane is evaluated in terms relative displacement of the particles (n.b. thus excluding rigid body motions) with the strain. The strain of the body along a plane normal to the x_i direction due to a force acting on the x_j direction is defined as

$$\varepsilon_{ij} = \frac{1}{2} \left(\frac{\partial u_i}{\partial x_j} + \frac{\partial u_j}{\partial x_i} \right) \quad \leftrightarrow \quad \varepsilon_{ii} = \frac{\partial u_i}{\partial x_i}. \quad (2.2)$$

In analogy with the stress, the strain is normal or axial provided that $i = j$, otherwise we talk about shear or transverse strain.

Given the definition of stress and strain, we can define the modulus of elasticity, the modulus of rigidity and the Poisson's ratio. The modulus of elasticity, or Young's modulus, is denoted as E and is measured in Pascal [$\frac{\text{kg}}{\text{ms}^2}$]. The Young's modulus is a measure of the

tensile stiffness of an elastic material along one direction and it evaluates how much the material can undergo an axial mechanical stress while exhibiting only elastic deformations (i.e. deformations for which the initial shape is completely recovered after the loads are removed [47]). The Young's modulus in the i direction is defined as the ratio of the axial stress σ_{ii} to the axial strain ε_{ii} through the Hooke's law, namely

$$\sigma_{ii} = E_i \varepsilon_{ii}. \quad (2.3)$$

The modulus of rigidity or Shear modulus, denoted as G , evaluates the resistance of the material to the deflection caused by shear stresses [47] and is measured in Pascal [$\frac{\text{kg}}{\text{ms}^2}$]. The Shear modulus on the plane $x_i x_j$ is defined as the ratio of the shear stress σ_{ij} to the shear strain ε_{ij} in the formulation of the Hooke's law for shear loads, namely

$$\sigma_{ij} = G_{ij} \varepsilon_{ij}. \quad (2.4)$$

The Poisson's ratio, denoted as ν , is a measure of the Poisson effect, which is the deformation of a solid body in a direction perpendicular to the specific direction of loading. The Poisson's ratio ν_{ij} is defined as the ratio of the transverse strain ε_{ij} to the axial strain ε_{ii} , namely

$$\nu_{ij} = -\frac{\varepsilon_{ij}}{\varepsilon_{ii}}. \quad (2.5)$$

As an example, the Poisson ratio $\nu_{x,y}$ measures how much a load in the x direction causes a deformation on the y direction.

Considering a 3D Cartesian reference system $[x, y, z]$, the relation between all the stresses and strains of a linear elastic body can be expressed extending the Hooke's law defined in Eq. (2.3) as

$$\begin{bmatrix} \varepsilon_{xx} \\ \varepsilon_{yy} \\ \varepsilon_{zz} \\ \varepsilon_{xy} \\ \varepsilon_{yz} \\ \varepsilon_{xz} \end{bmatrix} = \begin{bmatrix} C_{11} & C_{12} & C_{13} & C_{14} & C_{15} & C_{16} \\ C_{21} & C_{22} & C_{23} & C_{24} & C_{25} & C_{26} \\ C_{31} & C_{32} & C_{33} & C_{34} & C_{35} & C_{36} \\ C_{41} & C_{42} & C_{43} & C_{44} & C_{45} & C_{46} \\ C_{51} & C_{52} & C_{53} & C_{54} & C_{55} & C_{56} \\ C_{61} & C_{62} & C_{63} & C_{64} & C_{65} & C_{66} \end{bmatrix} \begin{bmatrix} \sigma_{xx} \\ \sigma_{yy} \\ \sigma_{zz} \\ \sigma_{xy} \\ \sigma_{yz} \\ \sigma_{xz} \end{bmatrix} \quad \text{or called } \begin{array}{l} \text{so called } \sigma_{zz} \\ \text{so called } \sigma_{xy} \end{array} \quad (2.6)$$

where the coefficients C_{ij} are the entries of the so called stiffness matrix and completely characterize the elasticity of an anisotropic material.

As a side note, notice that Eq. (2.3) and (2.4) are based on the assumption of a linear elastic material, which is an approximation of the real behavior of the material. The assumption of linearity is surely not satisfied for stress levels over the elastic limit, i.e. the maximum stress that can be applied to the body before the onset of permanent deformation. Nonetheless, many materials will deviate from Hooke's law well before the elastic limit is reached, thus defining a linearity region for which Hooke's law is valid.

2.1.2. Mechanical properties of wood

Wood belongs to orthotropic materials, which is a subclass of anisotropic materials. More in particular, anisotropy degenerates into orthotropy whenever it is possible to define three mutually-orthogonal axes with two-fold rotational symmetry inside the material structure.

As such, wood is characterized by different mechanical properties along the three different axes that identify its spatial directions, namely longitudinal (L), radial (R) and tangential (T). Fig. 2.2 illustrates the characteristic spatial directions of the wood. The longitudinal direction is parallel to the grains and the growth rings, the radial direction is perpendicular to both the grains and the growth rings, while the tangential direction is tangential to the growth rings and parallel to the grains.

Due to the symmetry, wood requires 12 out of 36 coefficients as entries of the stiffness matrix in order to be fully characterized, namely three Young's moduli E_L, E_R, E_T , three Shear moduli G_{LR}, G_{RT}, G_{LT} and six Poisson's ratios $\nu_{LR}, \nu_{RL}, \nu_{RT}, \nu_{TR}, \nu_{LT}, \nu_{TL}$. Therefore, considering a 3D Cartesian reference system $[x, y, z]$ corresponding to the three spatial directions $[L, R, T]$, for an orthotropic material the generalized Hooke's formula defined in Eq. (2.6) becomes

$$\begin{bmatrix} \varepsilon_{xx} \\ \varepsilon_{yy} \\ \varepsilon_{zz} \\ \varepsilon_{xy} \\ \varepsilon_{yz} \\ \varepsilon_{xz} \end{bmatrix} = \begin{bmatrix} \frac{1}{E_L} & -\frac{\nu_{LR}}{E_R} & -\frac{\nu_{TL}}{E_T} & 0 & 0 & 0 \\ -\frac{\nu_{RL}}{E_L} & \frac{1}{E_R} & -\frac{\nu_{TR}}{E_T} & 0 & 0 & 0 \\ -\frac{\nu_{LT}}{E_L} & -\frac{\nu_{RT}}{E_R} & \frac{1}{E_T} & 0 & 0 & 0 \\ 0 & 0 & 0 & \frac{1}{2G_{LR}} & 0 & 0 \\ 0 & 0 & 0 & 0 & \frac{1}{2G_{RT}} & 0 \\ 0 & 0 & 0 & 0 & 0 & \frac{1}{2G_{LT}} \end{bmatrix} \begin{bmatrix} \sigma_{xx} \\ \sigma_{yy} \\ \sigma_{zz} \\ \sigma_{xy} \\ \sigma_{yz} \\ \sigma_{xz} \end{bmatrix}, \quad (2.7)$$

where the null entries of the stiffness matrix represent uncorrelated stresses and strains.

Thanks to the internal symmetry of orthotropic materials it is possible to define the

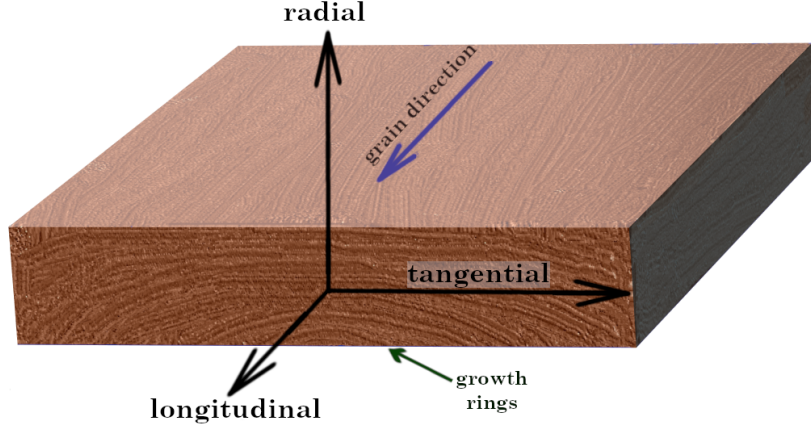


Figure 2.2: Principal axes of the wood. The direction of the grains is indicated by the blue arrow while the growth rings are pointed out by the green arrow. The longitudinal axis is parallel to the grains and the growth rings, the tangential axis is tangent to the growth rings and normal to the grains and the radial axis is normal both to the grains and the growth rings. Wood has different and independent mechanical properties along the three axes.

following equations:

$$\frac{\nu_{LR}}{E_L} = \frac{\nu_{RL}}{E_R}, \quad \frac{\nu_{LT}}{E_L} = \frac{\nu_{TL}}{E_T}, \quad \frac{\nu_{RT}}{E_R} = \frac{\nu_{TR}}{E_T}, \quad (2.8)$$

which clearly imply that three out of six Poisson's ratios are dependent variables, thus reducing the number of elastic constants needed to completely describe the stiffness of the wood from 12 to 9.

If we do not take into account any kind of energy loss due to damping, the knowledge of the stiffness matrix and the density ρ [$\frac{\text{kg}}{\text{m}^3}$] of the material allows to completely characterize the vibration of the body. Nevertheless, due to the resistance of the particles of the body at sliding one another, a certain amount of energy is always dissipated into heat during deformation. The loss of energy caused by this internal damping can be modeled by a viscoelastic material. Viscoelasticity is generally modeled through complex elastic constants, so that each elastic constant describes also the viscous behavior relative to its stress-strain couple. Viscous damping is usually expressed with the loss factor η_i , which is the ratio between the imaginary part and the real part of the given mechanical parameter.

2.2. Acoustical Properties of Wood

The acoustic performance of a given piece of wood mostly depends on its density, longitudinal Young's modulus and internal damping. From these variables, many physical descriptors characterizing the acoustics of wood have been proposed in the literature [3, 38, 39, 48, 60]. The most important parameters describing the acoustical properties of wood are the propagation speed of longitudinal waves along the grain, the characteristic impedance, the acoustic conversion efficiency [57] and the anisotropy ratio [38].

The **propagation velocity of longitudinal waves along the grain** c_L is referred to to the propagation velocity of longitudinal waves supported by a bar of the material under examination and is defined as

$$c_L = \sqrt{\frac{E_L}{\rho}}. \quad (2.9)$$

This physical quantity plays a major role in sound radiation. In order to understand why, let us consider the vibration of an infinite thin plate (n.b. remember that thin plates represent the first working stage for the soundboard of many stringed instruments). The thin plate supports the propagation of bending, torsional and quasi-longitudinal waves, but most of the sound radiation is due to bending vibration [14]. Bending waves are dispersive, which means that their propagation speed c_B depends from frequency. More in particular, c_B , the propagation velocity of bending waves, is directly proportional to the square root of the frequency and to c_L . We define as critical frequency the frequency value for which c_B is equal to the speed of sound in the air. Above the critical frequency the plate efficiently radiates sound, otherwise we will have inefficient sound radiation (i.e. the plate will radiate mostly evanescent waves, which are perceptible only in the near field of the plate). Since $c_B \propto c_L$, the critical frequency is inversely proportional to c_L . This implies that as c_L increases, the critical frequency and the frequency band characterized by inefficient sound radiation decrease. As we will see, c_L is used to compute many important acoustical parameters.

The **characteristic impedance** of the wood along the x_i direction is defined as the product between the density ρ and the propagation velocity of longitudinal waves the x_i direction. In particular the characteristic impedance along the longitudinal direction is expressed as

$$Z_L = \rho c_L = \sqrt{E_L \rho}. \quad (2.10)$$

This quantity measures the resistance of the medium to wave propagation and generally plays a major role when the vibrational energy is transmitted between two mediums. This

case scenario widely occurs in stringed musical instruments, where the vibration of the string is transmitted to the soundboard through the bridge. The transmission coefficient T along is defined as the ratio of the transmitted vibration to the incident vibration and can be expressed as

$$T = \frac{4Z_1Z_2}{(Z_1 + Z_2)^2}, \quad (2.11)$$

where Z_1 and Z_2 are the impedances of the two mediums. Studying Eq. (2.11) in function of Z_1 , one can easily see that the transmitted sound intensity is maximized for $Z_1 = Z_2$ and tends to zero for $Z_1 \ll Z_2$ or $Z_1 \gg Z_2$.

The **acoustic conversion efficiency** (ACE) was introduced by Yankovskii [58] as the ratio between the radiation ratio $R = \frac{c_L}{\rho}$ and the loss factor in the longitudinal direction η_L , namely

$$\text{ACE} = \frac{1}{\eta_L} \frac{c}{\rho} = \frac{R}{\eta_L} = \frac{1}{\eta_L} \sqrt{\frac{E_L}{\rho^3}}. \quad (2.12)$$

The **radiation ratio** represents a measure of how radiant is the wood and is proportional to the radiated sound intensity [48], whereas the loss factor affects the overall acoustical response of the wood. As said in [57], "if we wish to maximize the peak response of a soundboard or a bar, rather than the average response, we need to maximize the ratio of the radiation ratio to the loss coefficient", which is defined as the *ACE*.

The **relative acoustic conversion efficiency** (RACE) was introduced by Obataya [38] and is defined as follows:

$$\text{RACE} = \frac{c}{\eta_L}. \quad (2.13)$$

The RACE is related to the capability of transmitting vibration of the wood. The higher the RACE is, the more the material is a good conductor for sound. As such, the RACE is also referred to as "transmission parameter" [60].

The **anisotropy ratio** (AR) is a measure of the anisotropy of the wood and is defined as

$$AR = \frac{E_L}{G_{LR}} \frac{\eta_{LR}}{\eta_L}. \quad (2.14)$$

As predicted by Yano [59], an high anisotropy ratio reduces the power that a wooden plate radiates at high frequencies. Moreover, the anisotropy ratio is positively correlated with the ACE, meaning that woods with high *AR* are also acoustically efficient and vice versa, as such, it was proposed to employ this quantity for the evaluation of the acoustical quality of wooden soundboards of pianos [38].

2.3. Resonance Wood And Wood Selection

2.3.1. Different types of wood

Owing to its availability in nature and to the extremely wide range of mechanical properties amongst different species, wood is employed in many different fields, from industrial design to the construction of musical instruments. The classification of timber into species first involves the distinction between the two main families: hardwoods and softwoods.

Hardwoods mostly originate from deciduous trees that loose their leaves annually. Such trees tend to grow slowly, which implies that their wood is usually denser and more resistant to percussion with respect to softwoods. Examples of hardwoods are the oak and the mahogany. In musical acoustics, hardwoods are used to build the bars of xylophones (and wooden idiophones in general), the neck of instruments of the guitar family and the bows of instruments of the violin family.

On the other side, softwoods originate from evergreen trees, such as conifer or needle-bearing trees. Evergreen trees tend to grow faster than deciduous trees, thus their wood is usually less dense and more manipulable. Examples of softwoods are the spruce and the maple. In musical acoustics, softwoods are used for the construction of both the top-plates and the back-plates of picked or bowed stringed instruments and for building the soundboard of the instruments of the piano family. <

2.3.2. Resonance wood

The term "resonance wood" usually refers to the species of spruce traditionally employed for the top-plates of stringed instruments. Usually, the top-plate is the main radiating element of stringed instruments. As such, the material of the top plates should generally maximize sound radiation and sound transmission [60]. As such, the material of the top-plate should be characterized by low density ρ , high longitudinal Young modulus E_L , low shear modulus G_{LR} , low loss factor in the longitudinal direction η_L and high loss factor in the longitudinal to radial direction η_{LR} (see Eqs. (2.9), (2.10), (2.12) and (2.14)).

Spruce has traditionally been employed for top plates because it satisfies all those properties. Indeed, few wood species have material properties similar to the ones of spruce. As an example, for spruce the propagation velocity of longitudinal waves can go up to 6000ms^{-1} , while the species that support comparable propagation speeds are highly dense tropical hardwoods. As a result, spruce is characterized by a far higher radiation ratio with respect to other species [57].

In order to tackle the natural variability of the elastic properties of the material, resonance wood suppliers grade their wood based on its quality. Indeed, as Viala states "Resonance wood is a selected wood, and the variability is reduced due to the sorting of the logger. Most of the times, trunks showing nodes and irregular annual growth rings are rejected. The grain straightness is taken into consideration in the sorting process. The alignment of the grain of the wood has an impact on its material properties and its machinability" [54]. At the end of the quality grading process, resonance spruce is classified according to a nomenclature defined by the vendor.

2.3.3. Wood selection

The making of the soundboards of the guitar family instruments starts from wooden thin plates of resonance spruce that are called quarter-cut plates. The characteristic feature of these plates is that the wood grain direction (see Section 2.1) is oriented along the longitudinal axis of the plate. Even if the selection and the grading of the logger reduces the natural variability of the wood, the material parameters of resonance spruce are still considerably variable (i.e. 20% variability [8]). As such, quarter-cut plates are very different one another, even if they are cut from the same tree.

As a result, the first crucial step in instrument making is the choice of the wood. Indeed, luthiers usually carry out an additional selection process following quality, cost, artistic and workability criterions. Many research works investigate the selection process carried out by instrument makers, providing insight on the parameters evaluated by luthiers to assess the quality of a wooden sample [9, 12, 53].

It turns out that makers are not able to directly predict the acoustical and mechanical parameters, except for the density [9]. On the contrary, they carry out the selection process by evaluating with their senses some structural/anatomical features that are correlated to the material properties of the wood. The most important features are the colour of the wooden sample and the regularity of its growth rings. A brighter coloured wood generally indicates low density and structural integrity, whereas the more the growth rings are regular, the higher are the ACE and the anisotropy ratio of the wood.

The colour of the wood and the regularity of the growth ring are evaluated through the sense of sight, while density and damping are estimated through tactile and auditory rating, respectively. Visual rating seems to be more insightful for instrument makers with respect to auditory and tactile rating. That is, makers' decisions for optical quality can be predicted to some extent by the means of multiple linear regression, which implies that the anatomical/structural parameters related to vision are statistically significant

variables for the process of wood selection [9].

Moreover, Carlier conducted a socio-technical survey to evaluate violin makers' selection of wood, presenting the complete response of 15 luthiers [12]. The work clearly indicates that despite being interested on scientific approaches to characterize wood, few makers base their choice on measuring tools (only 17% rated it as important). Also the quality grades attributed by the suppliers resulted to be not important in their selection process (only 17% rated it as important).

2.4. Frequency Response Function

2.4.1. Features of a Frequency Response Function

The point Frequency Response Function (FRF) is the frequency domain complex-valued transfer function between an input and an output and its based on the assumption of linearity of the system. Usually, in the context of mechanical systems, the input is a force exerted at a given point of the body (i.e. the excitation point) while the output is the consequent vibration of another point (i.e. the measurement point).

The FRF is generally defined as

$$H_{ij}(j\omega) = \frac{X_j(j\omega)}{\mathcal{F}_i(j\omega)}, \quad (2.15)$$

where ω is the radians frequency, $\mathcal{F}_i(j\omega)$ is the spectrum of the force exerted at the excitation point i and $X_j(j\omega)$ is the spectrum of the vibration at the measurement point j in terms of either displacement, velocity or acceleration. As shown in Table 2.1, depending on which of these physical quantities is evaluated, the FRF can be either categorized as a receptance, a mobility or an inertance.

Name	Definition
Receptance	<i>Displacement/Force</i>
Mobility	<i>Velocity/Force</i>
Inertance	<i>Acceleration/Force</i>

Table 2.1: Different types of FRF. Depending on the physical quantity used to evaluate the motion of the body, the FRF can be categorized either as a receptance, a mobility or an inertance.

Since the point FRF is a complex-valued transfer function, it is usually represented in

terms of magnitude and phase, which are defined as

$$|H_{ij}(j\omega)| = \sqrt{\Re\{H_{ij}(j\omega)\}^2 + \Im\{H_{ij}(j\omega)\}^2}, \quad (2.16)$$

$$\angle H_{ij}(j\omega) = \tan^{-1} \left(\frac{\Im\{H_{ij}(j\omega)\}}{\Re\{H_{ij}(j\omega)\}} \right), \quad (2.17)$$

where $\Re\{H_{ij}(j\omega)\}$ is the real part of the point FRF, $\Im\{H_{ij}(j\omega)\}$ is the imaginary part of the point FRF, $|H_{ij}(j\omega)|$ is its magnitude and $\angle H_{ij}(j\omega)$ is its phase.

The FRF is a widely employed descriptor of the vibrational behaviour of solid bodies and allows to identify the natural frequencies and the damping characteristics of a structure. The natural frequencies, also called eigenfrequencies, are the frequencies at which a solid naturally vibrates when it is disturbed from its rest position by the application of an external force in empty (and undamped) space. Each eigenfrequency is associated to a modal shape and a modal damping ratio. The modal shape, also called mode of vibration, is the displacement field of the body at resonance. The points of zero displacement of a modal shape are called nodal points. The nodal points usually lie along lines that are the nodal lines of the given modal shape. The modal damping ratio is an adimensional factor that indicates the degree of viscous damping related to a mode of vibration in a damped environment. More details on modal shapes and modal damping ratios may be found in [35].

The value of the point FRF of a body is related to the eigenfrequencies, the modal shapes and the modal damping ratios of the measured body. Indeed, considering a mathematical model derived by means of modal superposition (Eq. 7.2262 in [35]) we have that

$$H_{ij}(\omega) \approx \sum_{n=1}^N \frac{\Phi_{ni}\Phi_{nj}}{\omega_n^2 + 2j\omega\xi_n\omega_n - \omega^2}, \quad (2.18)$$

where N is the number of modes taken into account, ω_n is the n^{th} eigenfrequency, ξ_n the n^{th} modal damping ratio and Φ_{ni} and the Φ_{nj} are the values of the n^{th} modal shape at the excitation and measurement points, respectively.

It is worth mentioning that when $\omega = \omega_n$, we have that

$$|H_{ij}(\omega_n)| \approx \frac{\Phi_{ni}\Phi_{nj}}{2\omega_n\xi_n}, \quad (2.19)$$

If either the excitation or the measuring point is on a nodal point of the n^{th} modal shape, the magnitude of the point FRF at ω_n will display a local minimum and we will say that

ω_n is an antiresonance for the considered point FRF. Instead, if this does not happen, ω_n will be a resonance for the considered point FRF and the magnitude of the point FRF will exhibit a local maximum at $\omega = \omega_n$. Moreover, the phase of the point FRF decreases of 180° in a uniform neighbourhood of the eigenfrequency if ω_n is a resonance, while it increases of 180° if ω_n is an antiresonance.

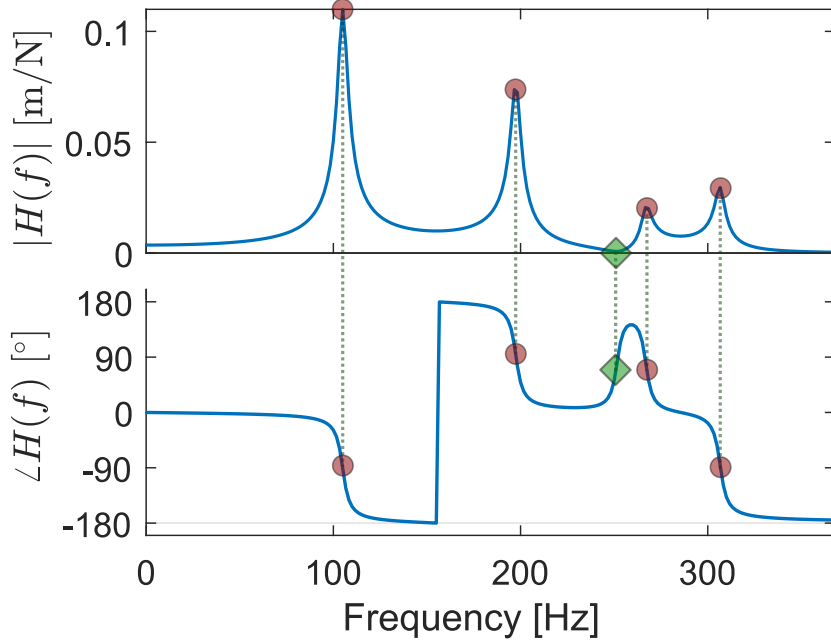


Figure 2.3: Example of magnitude (up) and phase (down) of a frequency response function. In particular, the FRF depicted in the figure is a receptance (i.e. displacement/force). We can see four resonances and one antiresonance, which are highlighted by four red circles and a green square, respectively. Each resonance corresponds to a local maximum in the magnitude plot and a decrease of 180° in the phase plot, whereas the antiresonance is associated to a local minimum in the magnitude plot and an increase of 180° in the phase plot.

Figure 2.3 depicts the magnitude and the phase of a point FRF. It is clearly visible that resonances (highlighted with a red circle) and antiresonances (highlighted with a green square) correspond to a local maximum or a local minimum in the magnitude plot and a decrease or an increase of 180° in the phase plot, respectively. Notice that whenever a resonance is close to an antiresonance we will not see a full increase/decrease of 180° , as their effect on the phase of the point FRF will balance one another.

2.4.2. Measurement of a Frequency Response Function

The type of force employed as input characterizes the test carried out to compute the FRF as follows:

- impact test, where the structure is excited with an impulsive force applied by a dynamometric hammer that is equipped with a sensor to measure the force;
- shaker test, where the structure is excited with a shaker. The shaker is a device that oscillates in accordance with a given signal. Usually, the signals employed to drive the shaker are white noise, sinusoids or sinusoidal sweeps.

It is important to point out that instrument makers usually perform impact tests and measure the vibration with accelerometers because of the low cost of the equipment. For this reason, in this thesis we perform hammer impact tests to measure the FRFs.

Accelerometers or laser scanners are usually employed to measure the vibration of the body both for impact tests and shaker tests. The disadvantage of using laser scanner as measuring device is mainly represented by the high cost of the tool, whereas the main drawback of employing accelerometers is that such sensors imply a local addition of mass to the system, thus altering the vibrational properties of the measured body. Moreover, while the laser scanner allows the simultaneous measurement of such points without any kind of mass loading of the body. In order to achieve similar results with accelerometers we need as many accelerometers as the number of points or to perform the roving hammer approach (i.e. in which the excitation point changes), which can be time consuming.

As for the excitation tool, the width of the frequency bandwidth that one is able to accurately measure with an impact test depends on the type of dynamometric hammer employed. Hammers with a hard tip yield force signals of shorter time duration and larger frequency bandwidth. As a result, the frequency range measurable with a hard tipped hammer is wider with respect to the one relative to hammers with a soft tip.

2.4.3. Estimation of a Frequency Response Function

The presence of systematic errors and noise can severely impair the correctness of the FRF computed with (2.15). As a result, the FRF is usually computed by the means of indirect estimators that decrease the effect of noise, but require multiple acquisitions at the same input-output pair [46]. In the following, the standard procedure for the estimation of the FRF relative to a single pair of excitation and measuring points and N acquisitions is illustrated.

The first step is the pre-processing of the acquired signals, which typically involves the windowing with an exponential filter. Successively, the Power Spectral Density (PSD) of the displacement G_{XX} , the PSD of the force G_{FF} and the Cross Spectral Density (CSD) between the force and the displacement G_{XF} are computed for each acquisition as

$$G_{XX}^{(i)}(j\omega) = \frac{X_i(j\omega)X_i^*(j\omega)}{2\omega} = \frac{|X_i(j\omega)|^2}{2\omega}, \quad (2.20)$$

$$G_{FF}^{(i)}(j\omega) = \frac{\mathcal{F}_i(j\omega)\mathcal{F}_i^*(j\omega)}{2\omega} = \frac{|\mathcal{F}_i(j\omega)|^2}{2\omega}, \quad (2.21)$$

$$G_{XF}^{(i)}(j\omega) = \frac{X_i(j\omega)\mathcal{F}_i^*(j\omega)}{2\omega}, \quad (2.22)$$

where i is the acquisition number and X_i^* and \mathcal{F}_i^* are the complex conjugates of the two spectra. The computed PSDs and CSDs are then averaged over the number of acquisitions as

$$\bar{G}_{XX}(j\omega) = \frac{1}{N} \sum_{i=1}^N G_{XX}^{(i)}(j\omega), \quad (2.23)$$

$$\bar{G}_{FF}(j\omega) = \frac{1}{N} \sum_{i=1}^N G_{FF}^{(i)}(j\omega), \quad (2.24)$$

$$\bar{G}_{XF}(j\omega) = \frac{1}{N} \sum_{i=1}^N G_{XF}^{(i)}(j\omega). \quad (2.25)$$

The PSD is defined as the Fourier transform of the autocorrelation of the signal and evaluates the power radiated by the signal in the frequency domain. Since it is proportional to the squared absolute value of the spectrum, the PSD emphasizes the peaks of the FRF with respect to its valleys, that are usually more noisy. Additionally, since the CSD is the Fourier transform of the cross-correlation between the two signals, it lowers the effect of the uncorrelated disturbances, such as white noise.

For the reasons listed in the previous paragraph, estimators of the FRF computed with the CSD and PSD are less noisy with respect to the FRF itself. Such estimators are the H_1 estimator, the H_2 estimator and the H_v estimator and they are all based on the hypothesis that the disturbance is purely additive. Indeed, the H_1 estimator assumes that noise is added only at the output, the H_2 estimator assumes that disturbances are present only at the input, while for the H_v estimator noise is present both at the input and the output. In this thesis, the estimation of the FRFs will be carried out by employing the

H_1 estimator, which is computed as

$$H_1(\omega) = \frac{\bar{G}_{XF}(j\omega)}{\bar{G}_{FF}(j\omega)}. \quad (2.26)$$

This implies that throughout this thesis we will assume that the force measurements are accurate and not noisy, whereas that all the noise in the FRF comes from the measurements of the accelerometer.

In order to estimate the quality of a given acquisition or the quality of the estimate of the FRF provided by the estimator, one can calculate the coherence function. As stated by the European Cooperation for Space Standardization in the standard ECSS-E-ST-32-11C, "the coherence function is a measure of the degree of linear, noise-free relationship between the measured system input and output signals at each frequency". The coherence function of the estimator is defined as

$$\gamma(\omega)^2 = \frac{\bar{G}_{XF}(j\omega)\bar{G}_{FX}(j\omega)}{\bar{G}_{XX}(j\omega)\bar{G}_{FF}(j\omega)}, \quad (2.27)$$

while the coherence function of a single acquisition is calculated in the same way, but substituting the PSDs and the CSD of the given acquisition to the averaged ones.

The coherence function varies between 0 and 1. A coherence close to 0 for a given frequency suggests that the estimated FRF is inaccurate since the measured output is mainly caused by noise or systematic errors, whereas a value close to 1 implies that the estimation of the FRF is not affected by disturbances and is thus reliable. A coherence function close to 1 at the resonances of the FRF indicates that the acquisition is satisfactory. If that is not the case, then we should either repeat the acquisition or discard it from the set of acquisitions used to compute the estimator of the FRF.

2.5. Rayleigh damping

Classical Rayleigh damping [44] is a widely employed damping model in the field of structural mechanics. Indeed, in the case of classical Rayleigh damping the damping matrix results from a linear combination of the mass matrix and the stiffness matrix of a multi-degree of freedom system (see [35] for a definition of such matrices). The control variables of the model, α and β , are the weights of the aforementioned linear combination.

A characteristic feature of this model is that the resulting modal damping ratios are frequency dependent. In particular, the modal damping ratios vary according to the

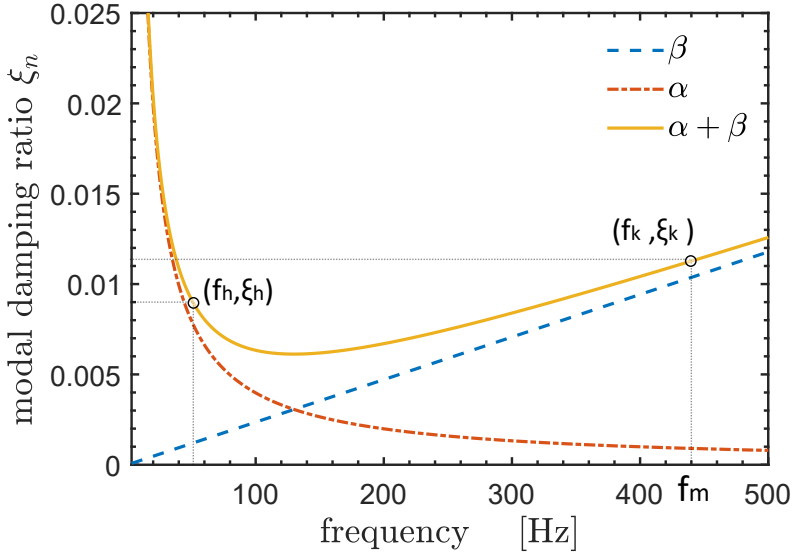


Figure 2.4: Modal damping ratio resulting from the Rayleigh damping model with $\alpha = 5[s]$ and $\beta = 5 \times 10^{-6}$. It can be seen that the resulting modal damping ratios mainly depend from α for lower frequency modes, whereas they mainly depend from β for higher frequency modes.

equation

$$\xi_i = \frac{1}{2} \left(\frac{\alpha}{\omega_i} + \beta \omega_i \right), \quad (2.28)$$

where ξ_i is the i^{th} modal damping ratio and ω_i is the i^{th} natural frequency of a body. Eq. (2.28) implies that the modal damping ratios result from the superposition of an hyperbolic relation (i.e. mass dependant damping) and a linear relation (i.e. stiffness dependant damping).

The values of α and β for modeling the damping of a given body can be inferred by if two modal damping ratios of the body are known. In particular, it is always possible to obtain a linear system of two equations of the form of Eq. (2.28) specialized for the modal damping ratios of the h^{th} and the k^{th} natural frequency, ξ_h and ξ_k . By solving this system one can easily obtain the values of α and β that yield the modal damping ratios ξ_h and ξ_k .

We can see that the modal damping ratios of lower frequency modes are mainly dependant from α , whereas the modal damping ratios of higher frequency modes mainly depend from β . Fig. 2.4 depicts the modal damping ratios resulting from Rayleigh damping versus the frequency for $\alpha = 5[s]$ and $\beta = 5 \times 10^{-6} [\text{s}^{-1}]$. The points denoted by the modal damping ratios ξ_h and ξ_k and their associated natural frequencies f_h and f_k are highlighted.

Rayleigh damping is widely used not only because of the simple identification of α and β , but also because of its numerical convenience. Indeed, differently from other damping models, the damping matrix provided by Rayleigh damping is quite regular. That is, the damping matrix is a linear combination of regular matrices. In particular, the mass matrix of a structure can be easily approximated with a diagonal matrix and the stiffness matrix is diagonal for isotropic materials, symmetric for orthotropic materials.

Notice that, despite being numerically convenient, this damping model is not suited to express the frequency dependence of the damping over an extended range of frequencies (i.e. more than 1000 Hz). Indeed, given α_0 and β_0 the values obtained for the modal damping ratios ξ_h and ξ_k , with $\omega_h < \omega_k$, modes with $\omega >> \omega_h$ or $\omega << \omega_k$ result over-damped. On the other hand, by choosing $\omega_h << \omega_k$, the frequencies inside the frequency range $[\omega_h, \omega_k]$ under-damped.

2.6. Wooden thin plates in free boundary conditions

Let us consider a quarter-cut plate (see Section 2.3) in free boundary conditions (i.e. suspended in the empty space) where longitudinal, radial and tangential directions are oriented on a Cartesian reference system (x, y, z) , respectively. The plate supports the propagation of bending, quasi-longitudinal and torsional waves (see [14] for more details). If the plate is excited by an impulsive force at a given point, the three types of wave named above will propagate in the plate. As a result, the plate will vibrate and the vibration will result from a point by point linear combination of the modal shapes of the plate.

The modal shapes of a quarter-cut plate in free boundary conditions are characterized by the number of nodal lines in the x direction m and by the number of nodal lines in the y direction n , that are used to define the so-called mode number for each mode of the plate [14]. Following the notation, we will refer to the eigenfrequencies of the plate and the associated modal shapes with the notation $f_{(m,n)}$ and (m, n) , respectively.

Figure 2.5 depicts the frequency response function of a wooden plate along with the modal shapes associated to each eigenfrequency. The nodal lines of the modal shapes correspond to the dark red areas, while the excitation and measuring point are depicted in white. As said in Section 2.4, the amplitude of the FRF at resonance is proportional to the product of the modal shape evaluated at the measurement and excitation point. As an example, the amplitude of mode $(2, 1)$ is the highest amongst the peaks of the FRF because the corresponding modal shape exhibits the highest displacement at the location of the excitation and measuring point.

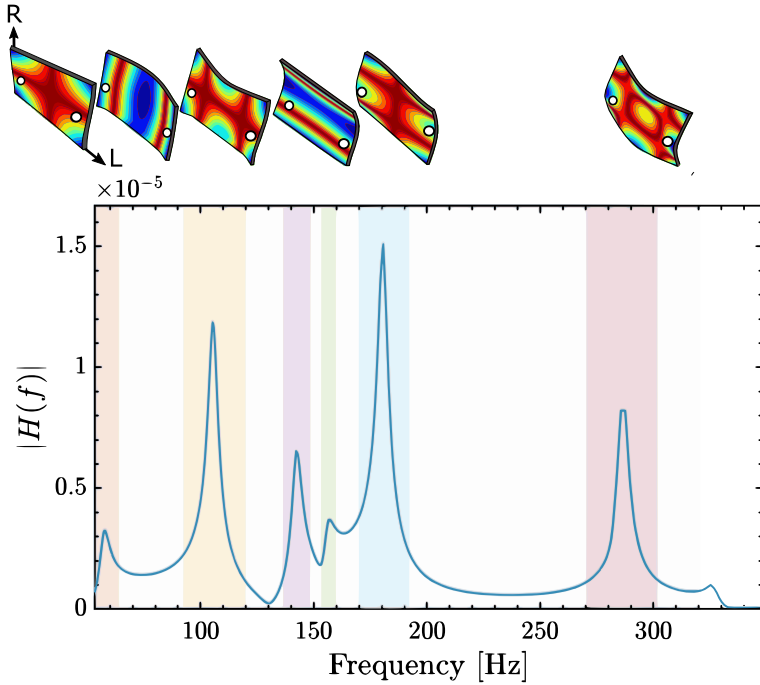


Figure 2.5: Example of point Frequency Response Function (FRF) of a wooden thin plate. The modes depicted in the figure are from left to right: (1, 1), (0, 2), (1, 2), (2, 0), (2, 1), (2, 2). The amplitude associated to each eigenfrequency is proportional to the product of the modal shape evaluated at the excitation and measuring points, that are depicted in white on each modal shape.

As a side note, since for a plate the thickness is negligible with respect to the other dimensions, the mechanical parameters defined along the thickness direction do not influence the overall vibration of the plate. In quarter-cut plates the tangential direction of the grain (T) is oriented along the thickness direction. Consequently, the material parameters that concern the tangential direction do not influence the vibration and can be neglect. Thus, the parameters of interest are 4 out of 9, namely the longitudinal Young's modulus E_L , the radial Young's modulus E_R , the longitudinal to radial Shear modulus G_{LR} and the longitudinal to radial Poisson ratio ν_{LR} .

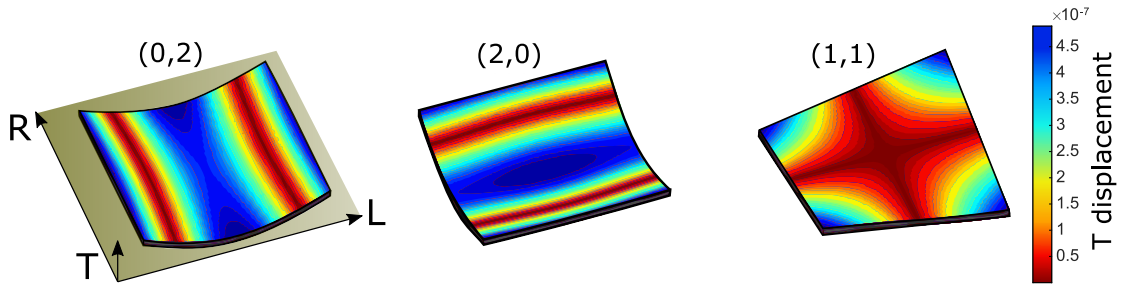


Figure 2.6: Characteristic modes of a wooden thin plate. From left to right we can see mode $(0, 2)$, mode $(2, 0)$ and mode $(1, 1)$, which are the fundamental longitudinal bending mode, the fundamental radial bending mode and the fundamental twisting mode, respectively. The first is related to the longitudinal Young modulus E_L , the second to the radial Young modulus E_R and the third to the longitudinal to radial shear modulus G_{LR} .

2.7. Non Destructive Evaluation of Wood

2.7.1. Caldersmith's formulas for wooden thin plates

The earliest vibration based non-destructive method for wood characterization was derived by Caldersmith, McIntyre et al. throughout the 80s [10, 30–32]. The proposed methodology is valid only for wooden rectangular thin plates in free boundary conditions and allows to estimate the longitudinal Young's modulus E_L , the radial Young's modulus E_R and the longitudinal to radial Shear modulus G_{LR} of the plate.

The proposed methodology is based on some equations that relate the frequency of certain characteristic modes of vibration to those material parameters, the density and the geometry of the plate. Such equations are derived from the Rayleigh theory on the vibration of wooden thin plates in free boundary conditions [44]. The characteristic modes, depicted in Fig. 2.6, are the following:

- mode $(0, 2)$, which is the fundamental bending mode along the grain and is related to the natural frequency $f_{(0,2)}$;
- mode $(2, 0)$, which is the fundamental cross-grain bending mode and is related to the natural frequency $f_{(2,0)}$;
- mode $(1, 1)$, which is the fundamental twisting mode and is related to the natural frequency $f_{(1,1)}$.

Mode $(0, 2)$ is mainly correlated to the longitudinal Young modulus E_L , while mode $(2, 0)$ and mode $(1, 1)$ are associated to the radial Young modulus E_R and the longitudinal to

radial shear modulus G_{LR} , respectively. Neglecting the effect of the Poisson ratios, the relation between the frequency of such modes, the geometry of the plate and the material parameters listed above are expressed as

$$E_L = \frac{0.096072\rho l^4 f_{02}^2}{h^2}, \quad (2.29)$$

$$E_R = \frac{0.096072\rho w^4 f_{20}^2}{h^2}, \quad (2.30)$$

$$G_{LR} = \frac{0.822\rho l^2 w^2 f_{11}^2}{h^2}, \quad (2.31)$$

where ρ is the density of the plate, h is the thickness of the plate and l and w are the dimensions of the plate in direction parallel and perpendicular to the grain direction, respectively. From Eqs. (2.29), (2.30) and (2.31) we easily see that the relation between the material parameters and the frequency of the characteristic modes is quadratic.

The estimation of the mechanical parameters by the means of such equations involves the identification of the characteristic eigenfrequencies. Such identification can be achieved either with Chladni patterns as described by Caldersmith [11] or with an automated algorithm that exploits the regularity of higher order eigenfrequencies [49]. Notice that this last methodology is more time consuming, as it requires the measurement of multiple FRFs.

2.7.2. Experimental/numerical techniques

A wide class of the techniques proposed for the vibration-based non-destructive characterization of wood are experimental/numerical techniques, where the numerical part is usually achieved with finite element method [62]. Typically, experimental/numerical techniques involve:

- an experimental measurement of the dynamical response of the wooden specimen, being either a FRF or the full displacement field of the body;
- a finite element model that simulates the experimental measurement;
- the definition of a loss function that evaluates how different is the simulated measurement with respect to the experimental one.

The material parameters of the body are estimated by minimizing the loss function and thus matching the simulated measurement with the experimental one. More in particular, the material parameters of the model are updated at each simulation step following a given

minimization algorithm (e.g. steepest descent [42] or Monte-Carlo minimization [43]). Thus, the whole process takes the name of Finite Element Model Updating (FEMU).

The main advantage of the FEMU approach is that FEM allows to model different boundary conditions on the same body [61], composite materials [28], arbitrary geometry bodies and complex structures, from violin top-plates [55] to the full body of a guitar [6].

Nevertheless, FEMU techniques are quite time-consuming. Indeed, in the best case scenario the numerical computation of the eigenfrequencies of a body takes 20 seconds. Supposing that the minimization of the loss function requires 400 iterations, it would take two hours to estimate the material properties of the body. Moreover the experimental measurement may be technically challenging to perform. The present work starts from this point and, in order to speed up material characterization, proposes a data-driven technique to identify the elastic properties of a wooden plate from a single measurement.

2.8. Concluding Remarks

In this Chapter, the basic concepts that will be extensively used in the thesis were given. First, an overview of the mechanical and acoustical properties of wood has been provided (Section 2.1 and Section 2.2, respectively). Subsequently, the concept of resonance wood has been presented along with a description of the wood selection process that instrument makers carry out before the making of the instrument (Section 2.3). Afterwards, the frequency response function is described in detail, as the FRF is one of the most diffused descriptor of the vibrational behaviour of solids and is widely used throughout this thesis (Section 2.4). Next, the Rayleigh damping model is illustrated as it is used to model damping throughout this thesis (Section 2.5). Following, the vibration of thin plates in free boundary condition is described since this thesis is focused on the characterization of wooden thin plates (Section 2.6). Finally, an overview of the main vibration based techniques for the non-destructive characterization of the wood is provided (Section 2.7).

3 | Generation and Analysis of the Dataset

In this chapter the methodology to generate the synthetic dataset that is employed to characterize the plates used for making the soundboard of classical guitar (i.e. classical guitar plates) is presented and the dataset is analysed. The dataset contains the first eigenfrequencies of the plate and the amplitude of a point FRF at the eigenfrequencies. First, we introduce classical guitar plates and briefly describe how the characterization of the material of such plates could enhance the design process of guitars. Secondly, we illustrate how the dataset is generated, illustrating how location of the points for which the FRF is evaluated is chosen and how input parameters of the dataset are sampled. At last, we propose an analysis of the dataset, focusing on the influence of the material parameters on the ordering of the modes along the frequency axis.

3.1. The guitar plate

In order to build the soundboards of the guitar family instruments, guitar makers start from two quarter-cut plates of spruce or cedar glued one another and then cut the soundboard from the obtained structure as shown in Fig. 3.1. As mentioned in the previous Chapter, the characteristic feature of these plates is that the wood grain direction is oriented along the longitudinal axis of the plate. We will refer to such plates as *classical guitar plates*.

Classical guitar plates come in standardized shape. The nominal dimensions are $(580 \times 220 \times 4)$ mm over the reference system (L, R, T) , where L , R and T refer to the grain direction, the cross-grain direction and the direction tangential to the grain, respectively. Deviations from the nominal geometry are accepted and quite common. Indeed, the corners of the plates are often not regular and plates sold by different sellers may have slightly different aspect ratios.

The material properties of classical guitar plates of the same species wood can vary greatly

from plate to plate, even for plates cut from the same tree. Guitar makers gain qualitative insight on the mechanical properties of the wooden sample via empirical methods, which enable them to make informed design decision (i.e. type of bracing [14], thickness of the plate and doming of the soundboard) during the building process of the guitar. An accurate estimation of the plate material properties would further enhance the quality of the design process carried out by guitar makers.

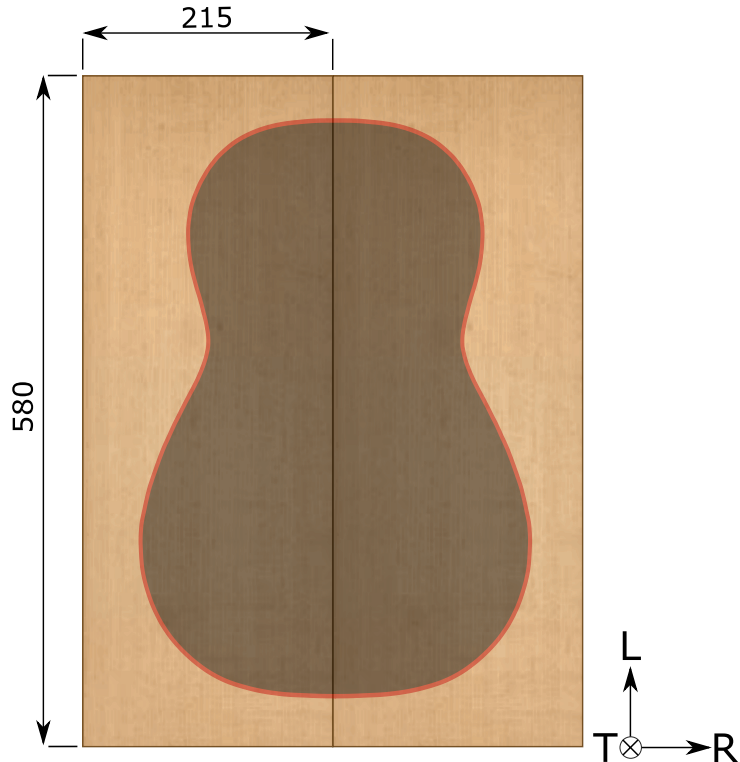


Figure 3.1: Guitar plates glued together to build a guitar soundboard. The geometry of a single guitar plate is standardized to $(580 \times 215 \times 4)$ mm. Small geometry variations are allowed. The wood grain direction is oriented along the longitudinal direction of the plate.

3.2. Dataset Generation

We aim to generate a dataset of synthesized vibrational data modeling the main features of a point FRF evaluated at prescribed points of the plate. A meaningful and compact representation can be achieved by approximating the FRF with the set of frequencies and amplitudes characterizing its peaks. In particular, we develop the dataset by computing the first 15 eigenfrequencies of the plate and the amplitude of a point FRF at the eigenfrequencies as the material properties and the geometry of the plate vary. Notice that only the resonances of the considered FRF (see Chapter 2 Section 2.4) will correspond to

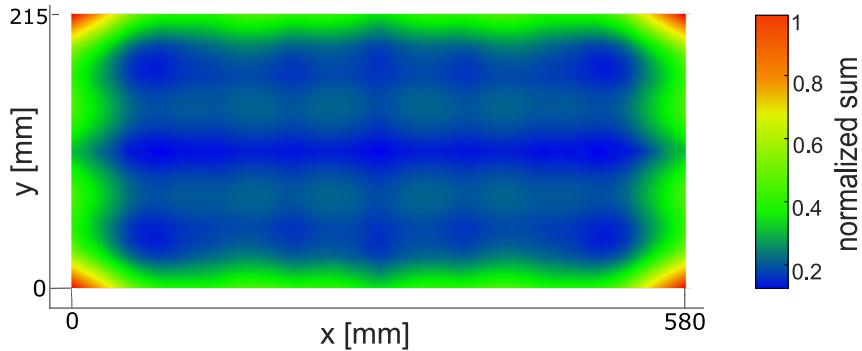


Figure 3.2: Normalized sum between the absolute value of the modal shapes relative to the first $S = 15$ eigenfrequencies obtained with the nominal material parameters of Red spruce and the standard geometry of classical guitar plates. The overall displacement field is maximum around the corners of the plate.

local maxima of the amplitude (i.e. peaks).

The dataset presented in this Chapter is built to characterize a set of 10 classical guitar plates of Red spruce. As such, some of its features come from measurements performed on this set of plates.

3.2.1. Geometry modeling and location of the measurement points

The definition of the finite element model involves the parametrization of the geometry of the plate, which is easily achieved with three parameters, namely the length l , the width w and the thickness h of the plates. Moreover, for simulating a FRF we need to define the location of the excitation and measurement points. In order to choose the location of such points, we analyse the first $S = 15$ simulated modal shapes obtained for the nominal material parameters of Red spruce [19] and the standard geometry of classical guitar plates.

Fig. 3.2 shows the normalized sum of the absolute value of the modal shapes. It is clearly visible that the overall displacement field is maximum around the corners of the plate. This suggests that by choosing a pair of measurement points located near the corners of the plate it is possible to simultaneously excite a great number of modes of vibration. Since in our dataset the geometry of the plate is variable, we define the location of the excitation and measurement points in function of the geometry parameters l and w . In particular, we chose to locate the excitation and the measurement points at 20mm from the edges of the bottom-left and top-right corners of the plate, as shown in Fig. 3.3.

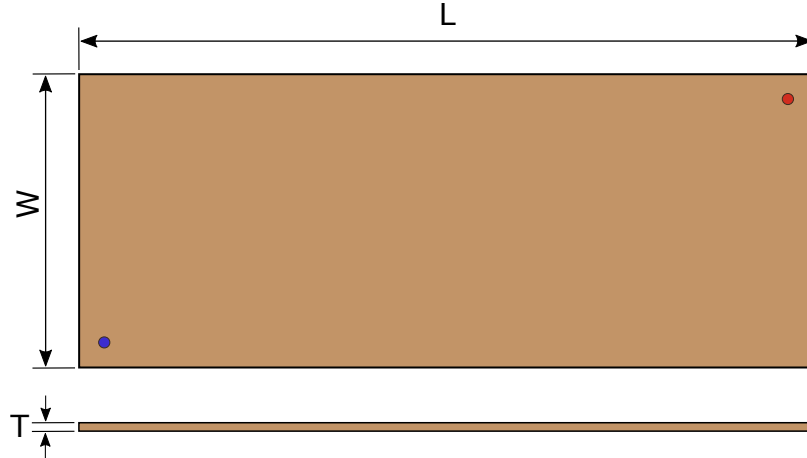


Figure 3.3: Schematic of the modeled guitar plates. The length, the width and the thickness of the plates vary throughout the dataset. The excitation and measurement points are depicted in blue and red, respectively. The points are placed at opposite corners of the plate at 20mm from the edges.

3.2.2. Sampling of the input parameters and simulations

In our dataset we vary the density, the material parameters (9 parameters) and the geometry parameters (3 parameters) of the plate. Moreover, we characterize the damping of the plate by means of the Rayleigh damping model (see Chapter 2 Section 2.5) and randomly sample its two control variables, α and β , thus including two additional parameters. So the total number of input parameters of the dataset is 15.

The density, the material parameters and the geometry parameters are randomly sampled by the means of 13 independent Gaussian random variables following the subsequent equation:

$$Y = Y_0(1 + \delta_Y), \quad (3.1)$$

where Y is an input parameter, Y_0 is its center value and δ_Y is a zero mean Gaussian random variable.

The center values of the density, longitudinal Young's modulus, radial Young's modulus and longitudinal to radial shear modulus (i.e. ρ_0 , E_{L_0} , E_{R_0} and G_{LR_0} , respectively) come from measurements performed on the set of 10 plates. In particular, ρ_0 is the average measured density, while E_{L_0} , E_{R_0} and G_{LR_0} the average estimates of the aforementioned elastic constants obtained with Caldersmith's formulas (see Chapter 2 Section 2.7). The center values associated to the remaining material parameters are the nominal elastic constants of Red spruce published by Hearmon [19]. The geometry parameters vary

around the nominal dimensions of classical guitar plates.

The center values of density, material parameters and geometry parameters are listed in Table 3.1, while the standard deviation of the associated Gaussian random variables are summarized in Table 3.2. The standard deviation of l , w and h corresponds the standard deviation of the measured geometry of the 10 guitar plates under study.

Density	Material Parameters			Geometry
$\rho_0 = 421 \frac{\text{kg}}{\text{m}^3}$	$E_{L_0} = 10.9 \text{ GPa}$	$G_{LR_0} = 580 \text{ MPa}$	$\nu_{LR} = 0.39$	$l_0 = 580 \text{ mm}$
	$E_{R_0} = 640 \text{ MPa}$	$G_{RT_0} = 26 \text{ MPa}$	$\nu_{RT} = 0.64$	$w_0 = 215 \text{ mm}$
	$E_{T_0} = 420 \text{ MPa}$	$G_{LT_0} = 590 \text{ MPa}$	$\nu_{LT} = 0.49$	$h_0 = 4 \text{ mm}$

Table 3.1: Mean values of the material and geometry parameters of the dataset. E_{L_0} , E_{R_0} and G_{LR_0} are the average values of the E_L , E_R and G_{LR} obtained with Caldersmith's formulas on our set of 10 classical guitar plates. The rest of the material parameters are the nominal elastic constants of Red spruce published by Hearmon [19].

Density	Young's Moduli	Shear Moduli	Poisson's Ratios	Geometry
$\hat{\sigma}_\rho = 0.1$	$\hat{\sigma}_{E_L} = 0.3$	$\hat{\sigma}_{G_{LR}} = 0.3$	$\hat{\sigma}_{\nu_{LR}} = 0.3$	$\hat{\sigma}_{l} = 0.01$
	$\hat{\sigma}_{E_R} = 0.3$	$\hat{\sigma}_{G_{RT}} = 0.3$	$\hat{\sigma}_{\nu_{RT}} = 0.3$	$\hat{\sigma}_{w} = 0.03$
	$\hat{\sigma}_{E_T} = 0.3$	$\hat{\sigma}_{G_{LT}} = 0.3$	$\hat{\sigma}_{\nu_{LT}} = 0.3$	$\hat{\sigma}_{h} = 0.075$

Table 3.2: Standard deviations associated to density, material parameters and geometry parameters.

The control variables of the damping model α and β are randomly sampled in a different way. In particular, α and β are associated with two independent uniform distributions following the subsequent equations:

$$\alpha = \alpha_0 (1 + U(-1, 1)) \quad [\text{s}^{-1}], \quad (3.2)$$

$$\beta = 2 \times 10^{U(-1, 1) - 6} \quad [\text{s}], \quad (3.3)$$

where $U(-1, 1)$ is a uniform random variable ranging in the interval $[-1, 1]$ and $\alpha_0 = 50$ is the center value of α . Notice that β ranges in the interval $(2 \times 10^{-7}, 2 \times 10^{-5})$ [s] such that the exponent is uniformly distributed in the range $[-7, -5]$.

For each occurrence of the dataset, we compute with Comsol Multiphysics® the first $S = 15$ eigenfrequencies of the plate along with the associated modal shapes and the value of the FRF at the eigenfrequencies with an *eigenfrequency study* and a *frequency domain study*, respectively. At each computation step the output data are stored in *.csv* files. At the end of the whole process, we obtain a dataset of 4500 occurrences containing

the eigenfrequencies and the amplitude of the point FRF at the eigenfrequencies, both sorted by the ascending order of the eigenfrequencies. Since the material properties of the plate are associated to Gaussian distributions with standard deviation equal to the 30% of the nominal values, we will refer to this dataset as the G_{30} dataset. It is worth to mention that the computation time associated to the generation of the G_{30} on a laptop is of ~ 24 hours.

3.3. Analysis of the dataset

The multidimensional mapping characterizing the input/output relation of the G_{30} is quite complex. One of the main factors complicating such relation is the varying ordering of the eigenfrequencies along the frequency axis. A study on cross laminated timber floor panels of dimensions $(7 \times 2.4 \times 0.28)$ [m] [40] has shown that the order of appearance of the eigenfrequencies along the frequency axis strongly depends from the material parameters. In the following we will refer to changes in the order of appearance of the eigenfrequencies in the frequency axis as *mode shifts*, as done in [40]. In order to investigate this aspect, we identify the modal shapes of the eigenfrequencies of each occurrence of the dataset, label the dataset by mode numbers and analyse the dataset before and after the identification process.

3.3.1. Modal shapes Labeling

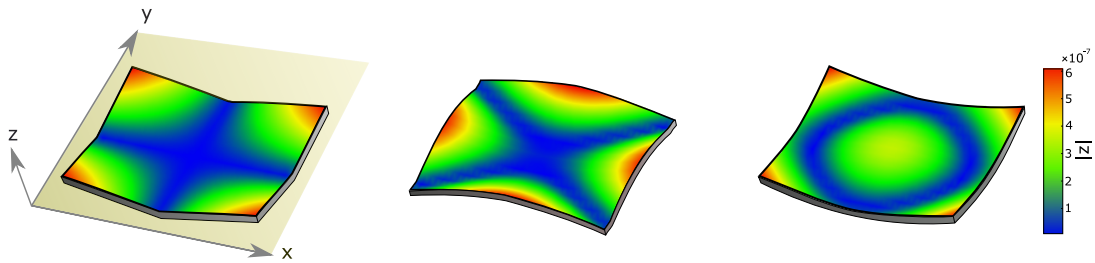


Figure 3.4: First three modal shapes of a Poisson plate, which is a plate that satisfies Eq. 3.4. The modal shapes of a poisson plate have fixed geometry and fixed order of appearance along the frequency axis. We can see, from left to right, the "cross" mode, the "x" or "saddle" mode and the "circle" or "breathing" mode.

Before carrying out the identification of the modal shapes we need to remove from the dataset very special cases, such as Poisson plates. A wooden plate is a Poisson plate when

its aspect ratio satisfies the following relation:

$$\frac{l}{w} = \sqrt[4]{\frac{E_L}{E_R}}. \quad (3.4)$$

The signature feature of a Poisson plate in free boundary conditions is that the modal shapes associated to the first three eigenfrequencies are fixed: the first natural frequency is associated to the "cross" mode, the second one is associated to the "X" or "saddle" mode, while the third one is associated to the "circle" or "breathing" mode.

Those modal shapes are shown in Fig. 3.4. In particular, the "X" mode and the "circle" mode are degenerate modes that cannot be associated to mode $(0, 2)$ or mode $(2, 0)$ of a normal plate. Thus, whenever one wants to identify the modal shapes of each occurrence in the dataset, Poisson plates are surely not recognized. For this reason, we chose to preliminarily discard all the Poisson plates from the dataset.

After the Poisson plates are removed, we can proceed with the identification of the modal shapes. The modal shapes are distinguished one another by comparing them to a reference set of 18 modal shapes obtained for the nominal values of Red spruce and labelled by mode numbers. The reference set of modal shapes is shown in Fig. 3.5.

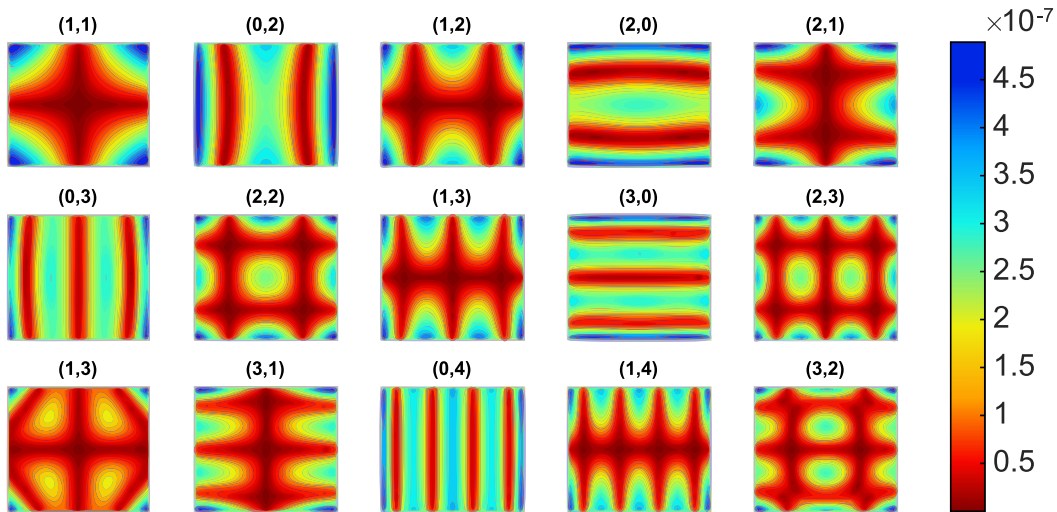


Figure 3.5: First 15 modal shapes of the reference set, which is obtained for the nominal parameters of the dataset (see Table 3.1).

The similarity between the resulting modal shapes $\hat{\Phi}$ and the reference set Φ is evaluated

in terms of Normalized Cross Correlation (NCC), which is computed as

$$\text{NCC}(\hat{\Phi}, \Phi) = \frac{\hat{\Phi}^T \Phi}{\|\hat{\Phi}\|_2 \|\Phi\|_2}. \quad (3.5)$$

The workflow of the modal shape identification process involves the following steps:

- resampling of the modal shapes in the dataset Φ into a rectangular grid of 35×15 points;
- resampling of the reference modal shapes $\hat{\Phi}$ into a rectangular and uniform mesh of 35×15 points;
- computation of the NCC between the modal shapes of the dataset and the reference set;
- labelling of each modal shape of the dataset Φ with the reference mode $\hat{\Phi}$ scoring the maximum NCC value;
- discarding all the occurrences of the dataset that display either repeated modes or a $NCC < 0.9$ for at least one mode.

After the identification of the modal shapes a dataset of 3530 occurrences and 15 columns is obtained (i.e. 3 modes of the reference set are discarded). Each column of the dataset corresponds to a given eigenfrequency. The columns are arranged in the subsequent order

$$\mathbf{o} = [f_{(1,1)}, f_{(0,2)}, f_{(1,2)}, f_{(2,0)}, f_{(2,1)}, f_{(0,3)}, f_{(1,3)}, f_{(2,2)}, f_{(0,4)}, f_{(2,3)}, f_{(1,4)}, f_{(3,0)}, f_{(3,1)}, f_{(3,2)}, f_{(2,4)}], \quad (3.6)$$

which is obtained by sorting the eigenfrequencies by the number of the FRF peak at which each eigenfrequency most frequently is (e.g. $f_{(1,1)}$ is the first because it is mostly associated with the first FRF peak, $f_{(0,2)}$ to the second and so on).

3.3.2. Effect of modes shifts

In the following, we will use roman numerals subscripts as notation to indicate the eigenfrequencies sorted by their ascending order in the frequency axis. Even if not all the eigenfrequencies will be resonances of the FRF, we will refer to the eigenfrequencies in ascending order as *peaks*. Moreover we will refer to the unprocessed G_{30} as the dataset *ordered by peaks* and to the G_{30} after modal shapes identification as the dataset *ordered by modes*.

First we evaluate the frequency distribution of the dataset before and after the labeling process. The left and the right part of Fig. 3.6 show the frequency distribution of the first

six peaks of the FRF and the frequency distribution of the first six modes, respectively. The distributions of the first three peaks and modes are quite similar. Indeed, the relative difference between the mean values of the first three peaks and modes is below 1%, while the relative difference between their standard deviation (n.b. in percentage of the mean) is below 6%. On the contrary, we can see great differences for the last three peaks and modes. In this case, the relative difference between the mean values ranges between 2.5% and 5.5%, whereas the relative difference between their standard deviation is between 8% and 24%.

The variations in the order of appearance of the modes along the frequency axis can be evaluated by looking at the occurrences of the dataset. Table 3.3 summarizes the correspondence between the first six modes of the dataset and the first six peaks of the FRF in ascending order. The rows and the columns of the table are associated to the modes and the peaks of the dataset, respectively. By looking at a single row of the table we can see how a mode is distributed between the FRF peaks. On the other hand, by looking at the columns of the table we can evaluate the composition of each peak in terms of modes. For f_I and f_{II} we have deviations from the most frequent ordering of modes (see Eq. (3.6)) only for $\sim 3\%$ of the occurrences. Deviations from the most frequent ordering happen much more frequently for f_{IV} , f_V and f_{VI} , namely for the $\sim 33\%$, $\sim 41\%$ and $\sim 48\%$ of the occurrences, respectively.

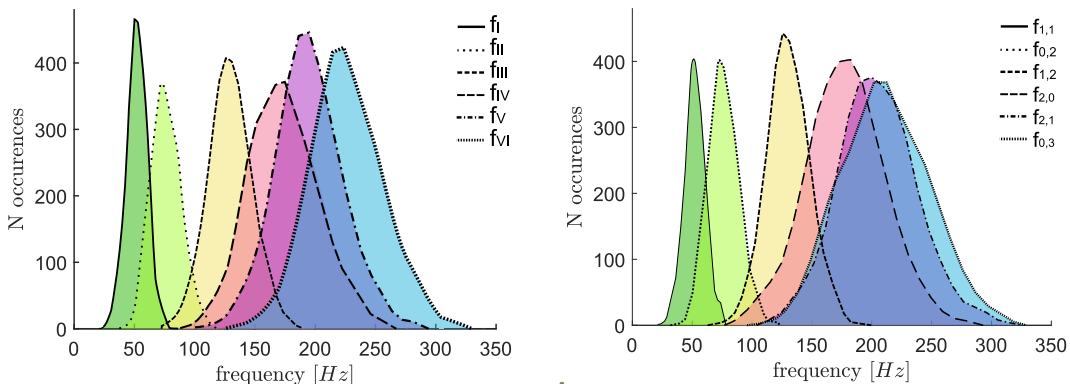


Figure 3.6: **Left:** distribution in frequency of the first six peaks in ascending order. **Right:** distribution in frequency of the first six modes after modal shapes identification (right).

As a last step, we compute the Pearson correlation coefficient between the inputs and the eigenfrequencies of both the G_{30} ordered by peaks and the G_{30} ordered by modes. The Pearson correlation coefficient measures the degree of linear relationship between

	f_I	f_{II}	f_{III}	f_{IV}	f_V	f_{VI}
$f_{(1,1)}$	3430	100	~	~	~	~
$f_{(0,2)}$	100	3430	~	~	~	~
$f_{(1,2)}$	~	~	3279	250	1	~
$f_{(2,0)}$	~	~	249	2386	871	24
$f_{(2,1)}$	~	~	2	52	2100	1435
$f_{(0,3)}$	~	~	~	842	529	1849

Table 3.3: Associations between the first six modes of the dataset and the first six peaks of the FRF in ascending order.

two variables and is defined as

$$r(x, y) = \frac{\sum_i (x_i - \bar{x})(y_i - \bar{y})}{\sqrt{\sum_i (x_i - \bar{x})^2 \sum_i (y_i - \bar{y})^2}}, \quad (3.7)$$

where $r(x, y)$ is the Pearson correlation coefficient between two variables x and y , \bar{x} and \bar{y} are the mean values of the variables and x_i and y_i are the i^{th} values of the variable in a given population. The Pearson correlation coefficient yields a value ranging in the interval $[-1, 1]$, where 0 indicates that the two variables are not linearly correlated, 1 stays for perfect positive linear correlation, and -1 is perfect negative linear correlation.

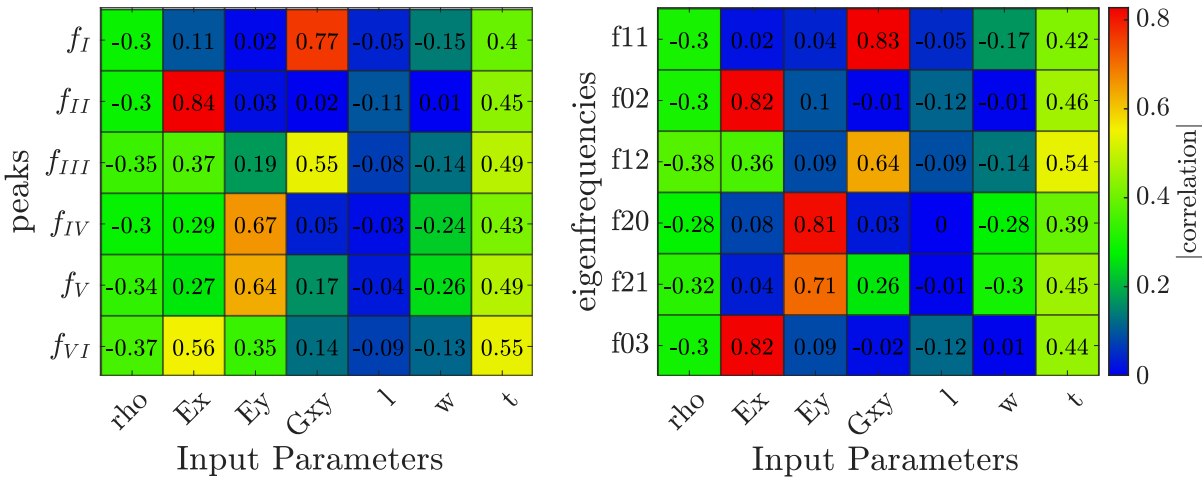


Figure 3.7: Pearson correlation coefficients between the eigenfrequencies and the density, the elastic constants E_L , E_R , G_{LR} and the geometry parameters. **Left:** dataset sorted by peaks. **Right:** dataset sorted by modes.

The left part Fig. 3.7 shows the Pearson correlation coefficients between the first six peaks and the density, the elastic constants E_L , E_R , G_{LR} and the geometry parameters, while the right part of Fig. 3.7 depicts the Pearson correlation coefficients between the first six

eigenfrequencies and the aforementioned input parameters. The differences between the two matrices stand out to the eye, especially if one looks at the column related to the elastic constants. On one hand, the plot related to the eigenfrequencies shows us that the characteristic eigenfrequencies (i.e. $f_{(1,1)}$, $f_{(0,2)}$ and $f_{(2,0)}$) and $f_{(0,3)}$ are mainly related to a single material parameter. On the other hand, mode shifts make the input/output relation of the dataset ordered by peaks a much more complex. Indeed, since each peak is "composed" by multiple modes most of the peaks are related to both E_L , E_R and G_{LR} .

In conclusion, the input/output mapping defined by the G_{30} is much more complex for the peaks rather than for the modes. This effect increases for higher order modes and peaks. That is, even more mode shifts occur for higher frequency modes (data not shown).

3.4. Concluding Remarks

In this Chapter, we discussed the methodology for generating the dataset that will be used to characterize wooden thin plates and provided an analysis of the dataset. First, the plates employed for guitar making are introduced (Section 3.1). Afterwards, the workflow related to the generation of the dataset is described in all its key steps, from the choice of the location of the measuring points, to how the input parameters vary throughout the dataset (Section 3.2). Subsequently, the dataset is analysed focusing on the ordering of the modes along the frequency axis (Section 3.3.1). As it can be seen from this last section, the input/output relation characterizing the dataset is quite complex. The dataset presented in this Chapter will be employed to train two predictors, one for frequency and another for amplitude. As we will see, a data model suited for predicting the outputs of this dataset is a feedforward neural network.

4 | Prediction of Frequency and Amplitude

In this Chapter the prediction of the outputs of the dataset (i.e. eigenfrequencies and amplitude of the point FRF at the eigenfrequencies) provided by two feedforward neural networks is studied. For the sake of simplicity, in the following we will always refer to the outputs of the G_{30} as frequency and amplitude. First, we introduce feedforward neural networks, defining the basic concept of topology of the neural network. Moreover, we describe how we implemented such neural networks. Secondly, we explain how the topology of the neural networks predicting frequency and amplitude is chosen. Finally, we evaluate the generalization (i.e. how the data model estimates out-of-sample occurrences) of the chosen data models.

4.1. Multilayer feedforward neural networks

After having analysed the main features of the G_{30} dataset, we study the accuracy of the regression of frequency and amplitude provided by two data models. In particular, we employ two Multilayer Feedforward Neural Network (MFNN) [51], one for frequency and one for amplitude.

We choose to employ multilayer feedforward neural networks since they are reckoned to be universal approximators of general mappings from one finite dimensional space to another [21]. In this thesis, the *Matlab®* Machine Learning Toolbox (NNTRAINTOOL) is used to implement and train the MFNN following the Levemberg-Marquadt algorithm [37]. The activation function of the neural network is the logistic sigmoid function and the loss function of the neural network is the mean squared error. The neural network is trained for 1000 epochs with early stopping [41]. In order implement early stopping, the dataset fed to the MFNN is randomly split into training set (80% of the occurrences), test set (10% of the occurrences) and validation set (10% of the occurrences). A detailed description of the toolbox can be found in [1, 4].

A diagram of a feedforward neural network is depicted in Fig. 4.1. The total number of layers \mathcal{L} and the number of neurons per layer \mathcal{M} define the topology (or architecture) of the MFNN. The accuracy of the MFNN can be enhanced by optimizing its topology, so that the expressivity of the network meets the complexity of the training data. Usually, the process of optimizing the topology of the MFNN is referred to as hyperparameters tuning of the MFNN.

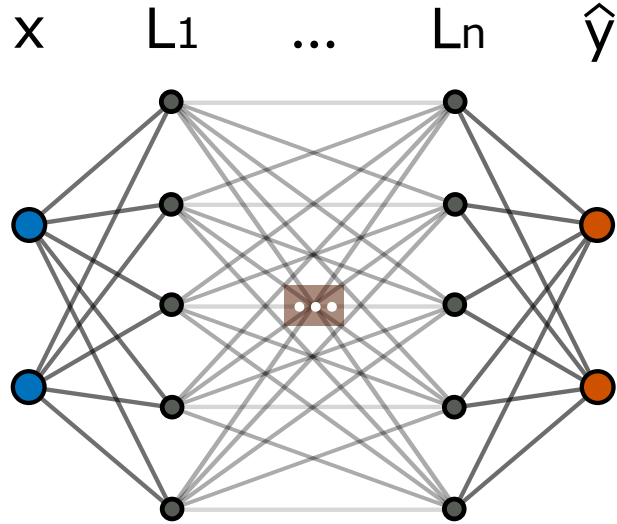


Figure 4.1: Diagram of a multilayer feedforward neural network. The neural network depicted in the figure has two inputs in the input layer x , two outputs in the output layer \hat{y} and \mathcal{L}_n hidden layers of five neurons each. The total number of layers and the number of neurons per layer define the topology of the neural network. In particular, the neural network depicted above is a $(5 \times \mathcal{L}_n)$ MFNN.

4.2. Choice of the Topology of the Neural Networks

In this section we will explain how the data models to estimate frequency and amplitude are chosen. The quality of the estimation provided by the MFNNs is assessed by evaluating the coefficient of determination R^2 , which provides a measure of how accurately the model replicates the observed outcomes [13, 16]. More specifically, we evaluate the average coefficient of determination defined as

$$\overline{R^2} = \frac{1}{15} \sum_{i=1}^{15} R_i^2, \quad (4.1)$$

where R_i^2 is the coefficient of determination related to the estimation of the i^{th} peak, either in frequency or in amplitude.

For training and testing the neural networks we randomly split the G_{30} into train set and test set containing the 90% and the 10% of the occurrences of the G_{30} , respectively. The \bar{R}^2 is computed on the test set. Notice that the train set is in turn randomly split into train, validation and test set as mentioned in the previous section. Thus, in this thesis two random splits are performed, namely an "external" split (n.b. done once) to compute the \bar{R}^2 and an "internal" split (n.b. each time a neural network is trained) to implement early stopping.

For the estimation of frequency we choose to employ a feedforward neural network with a single hidden layer of 17 neurons. It is worth to mention a single layer neural network with $N_p = n \text{ eigs} + 2$ neurons was also employed in [18] to predict the eigenfrequencies of a violin top plate. The (17×1) feedforward neural network yields $\bar{R}^2 = 0.988 \sim 0.99$. Given the accuracy of the network, there is no need to further optimize its topology.

On the contrary, in the case of amplitude we will need to optimize the topology of the neural network by tuning its hyperparameters. In order to do so, we carry out a grid search by varying \mathcal{L} between 1 and 4 with a step of 1 and \mathcal{M} between 2 and 64 with a step of 2. For each topology we train the MFNN with the amplitudes of the G_{30} expressed in dB and evaluate the \bar{R}^2 (see Eq. (4.1)) on the test set. The process is repeated for $N = 10$ realizations and the final results are obtained by averaging the \bar{R}^2 scored by each architecture.

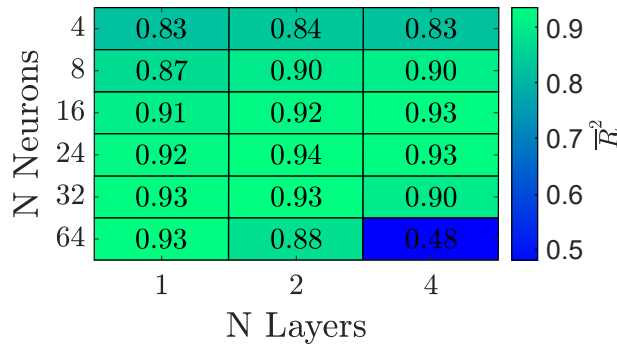


Figure 4.2: Hyperparameters tuning of the network trained with the G_{30} dataset. The matrices show the \bar{R}^2 defined in eq. (4.1) computed on the test set, obtained by randomly sampling the 10% of the occurrences of the G_{30} .

Fig. 4.2 summarizes the results of the hyperparameters tuning and indicates that the best MFNN for predicting the amplitudes is a (24×2) neural network, which yields $\bar{R}^2 = 0.94$. The decrease in the \bar{R}^2 that can be observed in the right-bottom part of the matrix is caused by overfitting.

As the word itself suggests, overfitting indicates that the weights of the neural network

are too exactly fitted on a finite set of data points. As a consequence, the model is able to excellently fit the occurrences of the training set, but totally fails to predict any occurrence that is not present in the training set. In other words, overfitting is characterized by a low value of the loss function on the train set and a high value of the loss function on the test set.

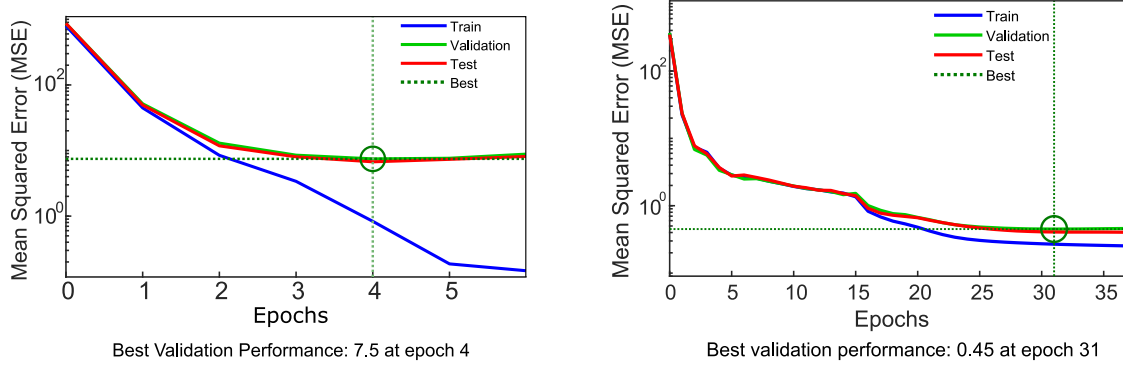


Figure 4.3: **Left:** train, test and validation losses versus the epoch number for a 64×4 MFNN trained with the G_{30} dataset. The model is too complex for the training data. As a result, overfitting is not avoided and the mean squared error on the validation set (i.e. the best validation performance) is high. **Right:** train, test and validation losses versus the epoch number for a (16×2) MFNN. The expressivity of the model meets the complexity of the training data. Therefore the discrepancy between the losses stays acceptable until the plateau is reached and the early stopping criteria are triggered, thus avoiding overfitting.

The left and the right part of Fig. 4.3 depict the train, test and validation losses versus the epoch number for a (64×4) MFNN and (24×2) MFNN, respectively. For both neural networks early stopping is triggered after that the loss function relative to the validation set consecutively increases for 6 epochs. We can see great difference in the training of the neural networks. For the (64×4) neural network we can see an abrupt decrease of the train loss for each epoch of training. Consequently, early stopping criteria are met after only 4 epochs, overfitting is visible starting from epoch 3 and the best validation performance (i.e. the minimum loss associated to the validation set) is high. On the contrary, for the (24×2) neural network the expressivity of the model is tuned with the complexity of the training set. Indeed, the low decrease of the loss function associated to a single epoch of training allows for a smooth reaching of the plateau. Overfitting occurs only after epoch 31 and the best validation performance is one order of magnitude lower with respect to the 64×4 MFNN.

4.3. Generalization

As a last step, we evaluate how the chosen neural networks estimate observations that fall outside the span that is well represented in the training set (i.e. for a Gaussian distribution the 95% of the observations are within the range [center value $\pm 2\sigma$]). In order to do so, both neural networks are tested with four U_s test sets of 300 occurrences each. The input parameters of the test sets are associated to uniform distributions centered around the nominal values shown in Table 3.1. Each test sets differs from the other in the distribution associated to the material parameters and the density. In particular, such distributions have an increasing span, namely set to the 25%, 50%, 75% and 95% of the nominal values, thus yielding the U_{25} , U_{50} , U_{75} and U_{95} test set, respectively. The span of the distribution associated to the length, the width and the thickness of the plates is the same for each U_s test set and is set to the 2%, 6% and 15% of the mean, respectively. Moreover, for each test set the control variables of Rayleigh damping are sampled according to Eqs.(3.2) and (3.3).

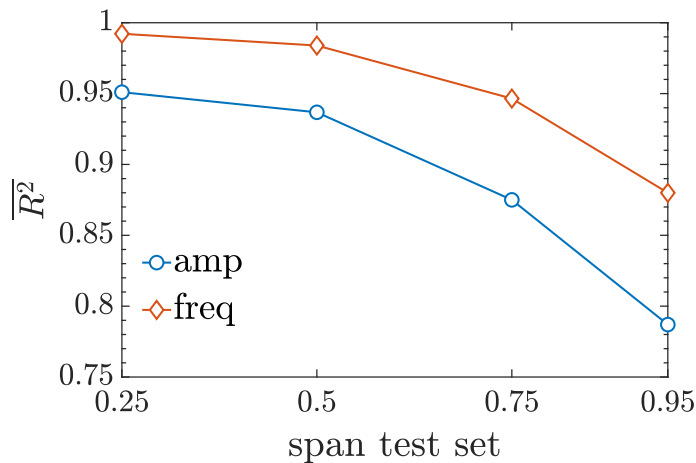


Figure 4.4: Results of the study performed to test the generalization of the MFNNs. Both neural networks are tested with four uniformly distributed U_s test sets. The U_s test sets are characterized by an increasing span of the distributions associated to the material parameters and the density, namely set to the 25%, 50%, 75% and 95% of the nominal values. The figure shows the mean coefficient of determination $\overline{R^2}$ (see eq. (4.1)) relative to the prediction of frequency and amplitude versus the span of the test set.

Fig. 4.4 shows the mean coefficient of determination $\overline{R^2}$ resulting from the testing process mentioned above, both for frequency and amplitude. As the span of the test set overcomes the 60% of the mean (i.e. the well represented range in the G_{30}), a drop of the $\overline{R^2}$ occurs, both for frequency and for amplitude. In particular, we can see that for frequency we

have $\overline{R^2} \approx 0.95$ for the U_{75} and $\overline{R^2} \approx 0.87$ for the U_{95m} whereas for amplitude we have $\overline{R^2} \approx 0.78$ for the U_{75} and $\overline{R^2} \approx 0.88$. This means that in the worst case scenario the MFNN predicting frequency can explain the 88% of the variance of the data, which is a good result. On the other hand, the MFNN predicting amplitude can explain the 78% of the variance of the data, yielding thus an acceptable prediction.

In conclusion, even if a larger error occurs, both MFNNs are able to provide a satisfactory estimate of observations that fall out the well represented range in their training set. It is worth mentioning that the natural variability of the material properties of Red spruce can be as high as 20% [8], which is widely covered from the G_{30} . As a result, we may conclude that the predictors presented in this Chapter can be safely employed to estimate the material properties of classical guitar plates.

4.4. Concluding remarks

In this Chapter we studied the prediction of the frequency and the amplitude provided by two feedforward neural trained with the dataset described in Chapter 3. First, feedforward neural networks are introduced, focusing on some of their key features, such as their topology and the method used for training them (Section 4.1). Secondly, the chosen topologies of the neural networks estimating the frequency and amplitude of the FRF peaks are given and motivated (Section 4.2). A (17×1) neural network and a (24×2) neural network are chosen for the prediction of the frequency and the amplitude of the FRF peaks, respectively. Finally, the generalization (i.e. how the neural networks estimate out-of-sample occurrences) of our networks is studied (Section 4.3). In conclusion, the neural networks presented in this Chapter are suited to characterize the material parameters of classical guitar plates, not only because their prediction is accurate, but also because out-of-sample occurrences are satisfactorily predicted.

5 | FRF2Params Method

In this Chapter, the data-driven technique for the characterization of the material of wooden thin plates that was developed in this thesis is presented. The methodology is denoted by the name *FRF2Params* and is inspired to FEMU approaches. Indeed, as FEMU techniques, the *FRF2Params* method is based on the minimization of a loss function. First, we provide an overview of the method, illustrating the pipeline of the method and its building blocks. Secondly, we describe in depth the minimization process, focusing on how the objective function of the minimization is computed. At last, we discuss the advantages of the method in terms of computation time.

5.1. Overview of the method

The *FRF2Params* method is a neural network based methodology that allows to simultaneously identify the plate material parameters. In order to apply the *FRF2Params* method on a plate one needs:

- the neural networks introduced in the previous Chapter. More specifically, a (17×1) MFNN for the prediction of frequency and a (24×2) MFNN for the prediction of amplitude;
- the frequency and the amplitude of the first $R = 12$ peaks of an experimentally measured FRF evaluated for the measurement points defined in Chapter 3;
- the dimensions of the plate;
- the density of the plate;
- a first guess of the plate material parameters (e.g. the nominal material parameters of Red spruce [19]).

The *FRF2Params* method is inspired to FEMU. As such, the heart of the technique is a minimization procedure. The main difference with FEMU is that instead of updating a finite element model, we update the input parameters of two neural networks. In particular, the minimization runs on the multidimensional space defined by the material parameters

only (i.e. 9 parameters). Indeed, the Ralyeigh damping variables, the geometry and the density of the plate are kept constant during each minimization.

To enhance the robustness of the solution, the final estimate of the material parameters is the average over the outputs of an arbitrary number N_r of subsequent runs of the minimization procedure, where each run starts with different initial conditions. More specifically, the minimizations differ one another for the value assigned to the density ρ . In particular, for each minimization:

- the density is associated to a Gaussian random variable centered on the measured density with a standard deviation equal to the 2.5% of its center value;
- the geometry parameters are fixed to the ones of the plate under analysis;
- the damping constants α and β are user defined.

On a laptop each minimization takes approximatively 40 seconds

It is worth to mention that the standard deviation of the material parameters coming from the minimizations provide an indication on the reliability of the estimates. In particular, if the standard deviation expressed in percentage of the average of a material parameter is significantly higher than the standard deviation associated to the density (2.5%), then the estimation of the given elastic constants is not much reliable.

5.2. Minimization

The objective function of the minimization is defined in the frequency-amplitude space. We will refer to the predictions of the neural networks as *estimated peaks* and to the peaks of the measured FRF as *measured peaks*. Notice that, while the measured peaks correspond to the local maxima of the FRF, some of the estimated peaks will be antiresonances for the considered FRF and are thus denoted by local minima instead of local maxima.

In order to tackle this issue, it is necessary to: **(i)** consider less measured peaks than estimated peaks during the minimization; **(ii)** develop a loss function that automatically discards the antiresonances. We achieve this last feature by defining a loss function that computes the frequency difference between each measured peak and the *nearest* estimated peak. The nearest estimated peaks are detected by evaluating the distance between measured and estimated peaks in the frequency-amplitude space. Since antiresonances and resonances display a high amplitude distance, antiresonances will never be marked as nearest estimated peaks. As a result, the detection of the nearest peaks is the key factor that allows us to employ a single point FRF to identify the material parameters of the

plate.

The minimization follows the pipeline shown in Fig. 5.1, which involves the following steps:

1. neural networks prediction of frequency and amplitude;
2. normalization of the amplitude of the *estimated peaks*;
3. computation of the distance between each *measured peak* and all the *estimated peaks*;
4. detection of the nearest *estimated peak* for each *measured peak*;
5. computation of the loss function as sum of the relative difference between the frequency of the measured peaks and the nearest estimated peaks;
6. updating of the material parameters following the Nelder-Mead simplex direct search algorithm [26];
7. iteration of steps 1 – 6 until termination criteria are satisfied.

As said in the previous section, the minimization runs on the multidimensional space defined by the material parameters only (i.e. 9 parameters). For each minimization the density ρ , the geometry parameters l , w and h and the control variables of Rayleigh damping α and β are fixed.

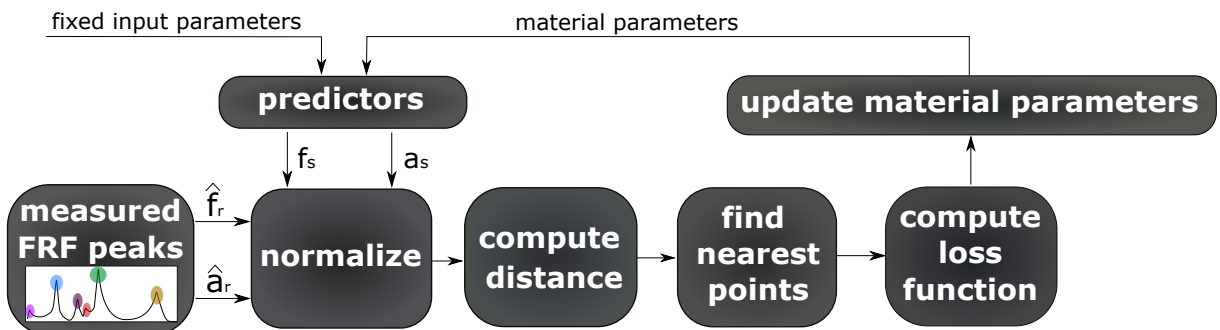


Figure 5.1: Iterative pipeline of a minimization procedure. The minimization runs on the multidimensional space defined by the material parameters only (i.e. 9 parameters). During the minimization the density ρ , the geometry parameters l , w and h and the control variables of Rayleigh damping α and β are fixed.

5.2.1. Computation of the loss function

Let us consider the first $R = 12$ measured peaks and $S = 15$ estimated peaks. We indicate the frequency and the amplitude of the r^{th} measured peak as \hat{f}_r and \hat{a}_r , with $r = 1, \dots, R$,

while the frequency and the amplitude of the s^{th} estimated peak will be indicated with f_s and a_s , with $s = 1, \dots, S$. Both measured and estimated amplitudes are expressed in dB.

First, since the measured amplitudes have a different mean value with respect to the ones obtained with FEM simulations due to a mismatch in the modeling of the excitation force (i.e. the amplitude is not the same, moreover in Comsol the force is an ideal Dirac impulse), we need to normalize the amplitudes of the estimated peaks as follows:

$$a_s^* = a_s + 20 \log_{10}(\gamma) \quad (5.1)$$

$$\gamma = \frac{\frac{1}{R} \sum_{r=1}^R \hat{a}_r|_{lin}}{\frac{1}{S} \sum_{s=1}^S a_s|_{lin}}, \quad (5.2)$$

where a_s^* is the s^{th} normalized estimated amplitude in dB, while $\hat{a}_r|_{lin}$ and $a_s|_{lin}$ are the r^{th} measured amplitude and the r^{th} estimated amplitude in linear scale, respectively. The ratio between the average of the measured amplitudes and the average of the estimated amplitudes γ is converted in dB scale and added (n.b. which is equal to a multiplying in linear scale) to a_s .

Fig. 5.2 depicts both estimated and measured peaks before and after the normalization. In particular, the left part of Fig. 5.2 shows the peaks before the normalization, while the right part of Fig. 5.2 shows the effects of the addition of γ to the amplitude of the *estimated peaks*. It can be seen that after the normalization the average amplitude of the estimated and measured peaks are comparable.

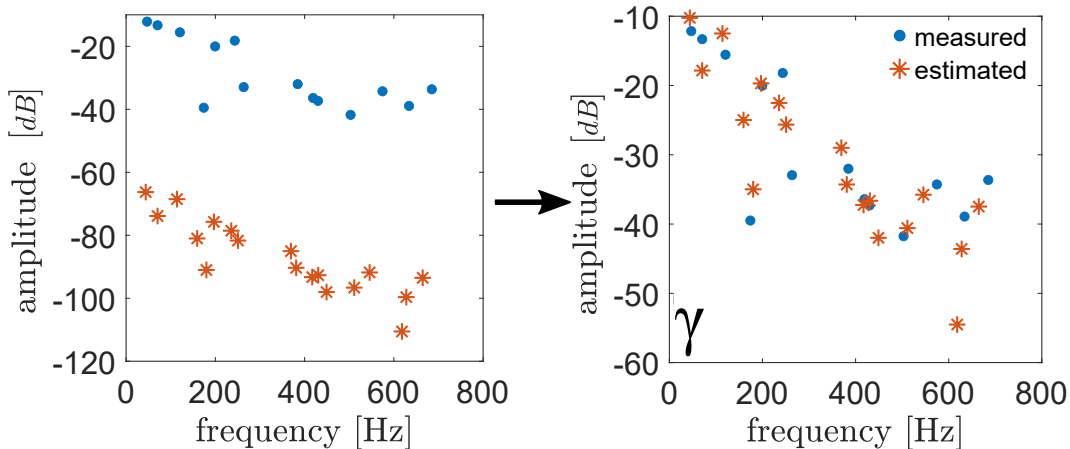


Figure 5.2: Normalization between estimated FRF peaks and measured FRF peaks. **Left:** measured FRF peaks and estimated FRF peaks without any modification. **Right:** resulting peaks after the normalization (see Eqs. (5.2) and (5.1)).

Successively, we compute the matrix $D \in \mathbb{R}^{R \times S}$ of the euclidean distances between all the combinations of measured peaks and estimated peaks. A single entry of this matrix is calculated as

$$[D]_{r,s} = \sqrt{(\hat{f}_r - f_s)^2 + (\eta(\hat{a}_r - a_s^*))^2}, \quad r = 1, \dots, R \quad s = 1, \dots, S, \quad (5.3)$$

$$\eta = \frac{1}{R} \sum_{r=1}^R \frac{\hat{f}_r}{\hat{a}_r} \quad (5.4)$$

where η is used to give the same weight to frequencies and amplitudes in the computation of the distance. The product of both amplitudes with the constant η allows us to give the same weight to frequency and amplitude in the computation of the distance. Indeed, the frequency axis has a wider range with respect to the amplitude axis. If we did not introduce the constant η frequency differences would have been prioritized with respect to amplitude differences in the computation of the distance, which is not what we want.

We detect for each measured peak $\bar{r} = 1, \dots, R$ the index of the closest estimated peak as

$$\chi_{\bar{r}} = \arg \min_s \{ [D]_{r,s} \mid r = \bar{r} \wedge s = 1, \dots, S \}, \quad (5.5)$$

such that $\chi \in \mathbb{R}^{R \times 1}$.

We can now compute the loss function \hat{L}_2 as

$$\hat{L}_2 = \sum_{r=1}^R w_r \left(\frac{\hat{f}_r - f_{\chi_r}}{\hat{f}_r} \right)^2 + J_\chi, \quad (5.6)$$

$$w_r = \begin{cases} 1.2 & \text{if } r \leq 5 \\ 1 & \text{otherwise} \end{cases}, \quad (5.7)$$

$$J_\chi = (R - A)^2, \quad (5.8)$$

where:

- f_{χ_r} is the frequency of the nearest estimated peak with respect to the r^{th} measured peak;
- w_r is the r^{th} entry of a vector of weights of length R \mathbf{w} and allows to slightly prioritize the matching of lower frequency modes with respect to the matching of higher frequency modes;
- A is the number of distinct values contained in χ and J_χ is a penalty function that

penalizes the condition in which two or more measured peaks are associated to the same estimated peak . As an example, if $A = R$, each *measured peak* is associated to a single *estimated peak* and $J_\chi = 0$. If $R - A = 1$, two *measured peaks* are associated to the same *estimated peak* and $J_\chi = 1$. If $R - A = 2$, either three *measured peaks* are associated to the same *estimated peak* or four *measured peaks* are associated to two *estimated peaks* and $J_\chi = 4$, and so on.

5.2.2. Model updating

The minimization is achieved by employing the Matlab[®] function *fminsearch*, which applies the Nelder-Mead simplex direct search algorithm [26]. The Nelder-Mead simplex direct search is a popular algorithm for multidimensional unconstrained minimization without derivatives. The fact that there is no need to compute the gradient makes this method suitable for our minimization problem, since the loss function includes a discontinuous loss functional.

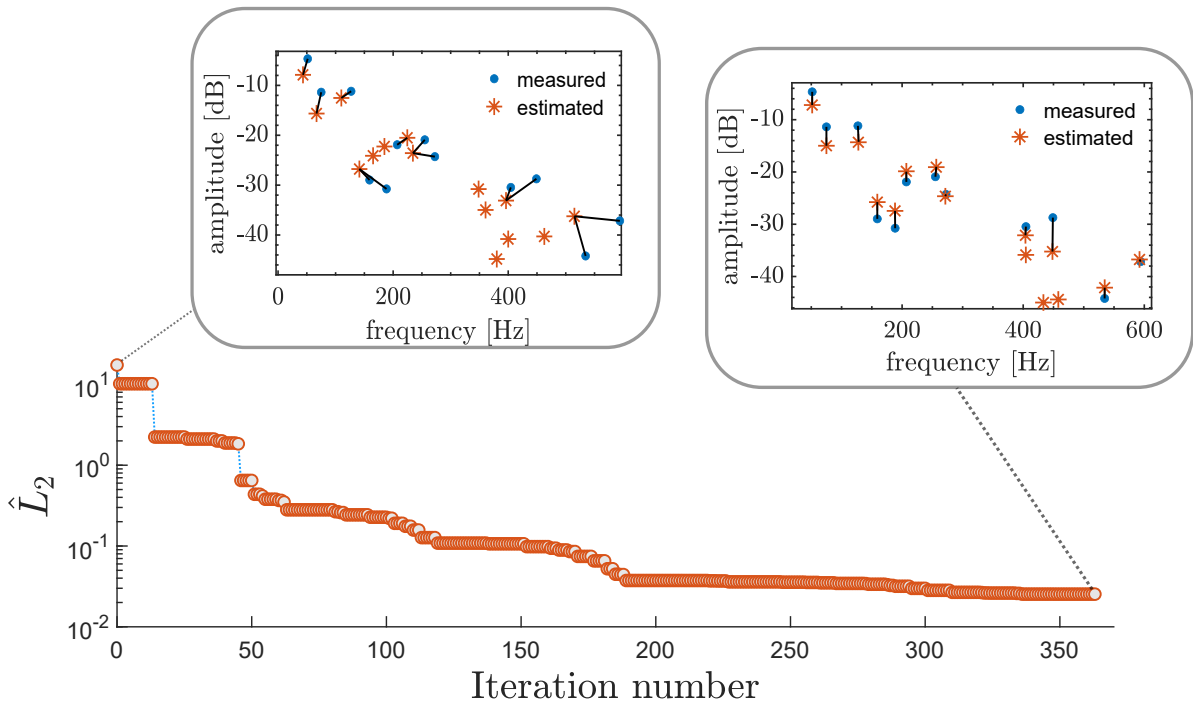


Figure 5.3: Evolution of the loss function for a single minimization task. In the left part of the figure we can see the *estimated peaks* and *measured peaks* corresponding to the first guess of the material parameters, while in the right part we can see how the frequency/amplitude pairs are distributed at the end of the minimization. The black lines connect each *measured peak* to the closest *estimated peak*.

Fig. 5.3 depicts the evolution of the loss function for a minimization procedure. In the

left part of the figure we can see the *estimated peaks* and *measured peaks* corresponding to the first guess of the material parameters, while in the right part we can see how the frequency/amplitude pairs are distributed at the end of the minimization. The black lines connect each *measured peak* to the closest *estimated peak*. For the first guess we have four couples of *measured peaks* associated to the same *estimated peak*, while after the minimization we have a 1 : 1 association between the peaks. Indeed, we can see three major jumps that correspond to the discontinuous variations of the cost functional J_χ . The loss function shows a fast convergence, going from $\hat{L}_2 = 17.37$ to $\hat{L}_2 = 0.025$ in only 363 iterations.

As it can be seen from Fig. 5.3, the Nelder-Mead simplex direct search proves to be an effective and efficient minimization algorithm. Indeed, the minimization satisfies the termination criteria in relatively few iterations.

The termination criteria for the Matlab® function *fminsearch* are two and must be met together. The first termination criterion, denoted as Tol_X , is a lower bound on the variation that the variables of the objective function (i.e. the material parameters) can undergo from a step of minimization to the subsequent one. For multidimensional minimization (such as in our case) we have that $Tol_X = ||X_{i+1} - X_i||_2$, where i is the number of the iteration and X_i is the a vector containing the values of the variables of the objective function for each iteration. The second termination criterion, denoted as Tol_{Fun} , is the minimum change in the value of the objective function for two adjacent iterations. For our implementation we set $Tol_X = 1 \times 10^5$ and $Tol_{Fun} = 1 \times 10^{-4}$.

5.3. Advantages of the method

As most of FEMU approaches, the *FRF2Params* method enables the simultaneous estimation of the material parameters of the plate. The main advantage of the *FRF2Params* method with respect to FEMU approaches is that neural networks lead to a great reduction in computational time without a significant loss of accuracy. To quantify the improvement in computational time we evaluate the speed gain G_p , which is defined as

$$G_p = \frac{t_{FE}}{t_P}, \quad (5.9)$$

where t_{FE} is the time that a finite element solver takes to compute either the first 15 eigenfrequencies of the plate or the amplitude of the point FRF at such eigenfrequencies, whereas t_P is the inference time of the MFNN that estimates either frequency or amplitude.

Table 5.1 shows the inference time of both predictors t_P , the inference times of the finite element model t_{FE} , both for frequency and amplitude, and the corresponding speed gain G_p . We can see that t_P is three orders of magnitude lower than t_{FE} for both frequency and amplitude. Thus, we can safely conclude that *neural network updating* techniques guarantee a gain of three orders of magnitude in terms of computation time with respect to FEMU techniques.

Notice that the inference times shown in Table 5.1 are associated to the calculations of a laptop that is not performing any parallel computation (other than the ones required by the operative system). Anyhow, the speed gain can be considered as a relative measurement, so it allows us to evaluate the improvement independently from the calculator employed to perform the computations.

	t_{FE} [ms]	t_p [ms]	G_p
frequency	15525	17	913
amplitude	25820	19	1359

Table 5.1: Comparison between the computation time associated to the calculations of the finite element model of the plate and the inference time of the neural network, both for frequency and amplitude. The third column of the table expresses the speed gain defined in Eq. (5.9).

5.4. Concluding Remarks

In this Chapter we presented and discussed the *FRF2Params* method, which is the minimization based technique developed in this thesis to characterize wooden thin plates. First, an overview of the method is given. The building blocks of the method (n.b. which include the neural networks presented in the previous Chapter) are introduced and the workflow that leads to the final estimation of the material properties is illustrated (Section 5.1). Secondly, a focus on the minimization procedure is proposed. In particular, the objective function of the minimization is defined and its evolution during a minimization is shown (Section 5.2). Finally, the advantages of the *FRF2Params* method in terms of gain of computational time are discussed by comparing the inference time of the neural networks with the computation time of a finite element model.

6 | Results of the FRF2Params method

In this chapter the *FRF2Params* method is applied on a set of 10 guitar plates and the results are discussed. First, we introduce the aforementioned set of guitar plates, describing how the measurement of their geometry, density and point FRF were performed. Secondly, we present the estimations of the material properties obtained with the *FRF2Params* method on the set of plates and provide a discussion of the results.

6.1. Materials

The *FRF2Params* method is employed to estimate the material properties of a set of 10 classical guitar plates made of Red spruce. The plates are book-matched, i.e. cut from the same chunk of wood. Plates belonging to the same cut are supposed to be glued together by the guitar maker. Thus, we will label the plates by the number of the pair to which they belong (which is arbitrary) followed by either L or R subscript, which indicates the left and the right side of the glued structure, respectively.

Figure 6.1 depicts the set of guitar plates. The plates display a different degree of geometry regularity, in particular: (i) the pairs $1_L/1_R$ and $4_L/4_R$ display relevant irregularities at their corners; (ii) the pair $3_L/3_R$ shows moderate imperfections (3_L has irregular edges, while 3_R does not); (iii) the pairs $2_L/2_R$ and $5_L/5_R$ have either no defects or neglectable defects.

We measured the geometry and the density of each plate. Length and width are measured with a ruler (precision of ± 1 mm), thickness is measured with a decimal vernier caliper (precision of ± 0.1 mm) while the mass M is measured with a weighing machine (precision of ± 1 g). Length, width and mass are measured $N_1 = 5$ times, while thickness is measured $N_2 = 10$ times. The uncertainty related to the measurement of the density is derived from the standard deviations of the measurements of length, width, thickness and mass (σ_l , σ_w , σ_t and σ_M) by applying the variance formula [24] as specified in the following.



Figure 6.1: Set of 10 classical guitar plates made of Red spruce that we measured and characterize. We can see that most of the plates exhibit an irregular geometry, in particular: (i) the pairs $1_L/1_R$ and $4_L/4_R$ display relevant irregularities at their corners; (ii) the pair $3_L/3_R$ shows moderate imperfections (3_L has irregular edges, while 3_R does not); (iii) the pairs $2_L/2_R$ and $5_L/5_R$ have either no defects or neglectable defects.

First, we derive the standard deviation σ_v associated to the volume $v(l, w, h) = lwh$ as

$$\sigma_v = \sqrt{\left(\frac{\partial v}{\partial l}\right)^2 \sigma_l^2 + \left(\frac{\partial v}{\partial w}\right)^2 \sigma_w^2 + \left(\frac{\partial v}{\partial t}\right)^2 \sigma_t^2}, \quad (6.1)$$

and then we derive the standard deviation σ_ρ associated to the density $\rho(v, M) = \frac{v}{M}$ as

$$\sigma_\rho = \sqrt{\left(\frac{\partial \rho}{\partial m}\right)^2 \sigma_m^2 + \left(\frac{\partial \rho}{\partial v}\right)^2 \sigma_v^2}. \quad (6.2)$$

The standard deviation associated to the density represents the uncertainty of the measurement $\Delta\rho$. The measured values of geometrical parameters, mass and density of each plate are reported in Table 6.1 along with the uncertainty associated to the density measurement (in percentage).

For each plate we estimate the point FRF related to the measurement points defined in Section 3.2 by accelerometer-based hammer impact testing. The experimental setup for measuring the FRF involves a wooden structure that holds the dynamometric hammer and two rubber bands that support the plate, simulating free boundary conditions. Each plate is excited and measured 6 times by acquiring the force of the hammer and the consequent acceleration of the plate. The point FRFs are estimated with the H_1 estimator as described in Section 2.4. The peaks of the magnitude of each point FRF are successively detected performing peak analysis.

sample	l [mm]	w [mm]	h [mm]	M[g]	ρ [$\frac{\text{kg}}{\text{m}^3}$]	$\Delta\rho$ [%]
1_L	580	213	4.8	236	397	4.1
1_R	580	211	4.6	248	441	4.5
2_L	580	215	5.0	256	418	3.0
2_R	580	217	4.7	257	434	3.3
3_L	580	217	4.2	235	445	2.9
3_R	580	218	5.0	253	410	3.1
4_L	576	216	4.6	226	394	3.2
4_R	577	209	4.4	211	398	5.0
5_L	581	218	5.0	273	440	3.1
5_R	581	217	5.0	269	435	2.4

Table 6.1: Measured values of the geometry and density of each plate along with the uncertainty associated to the measurement of the density. The measurements of length, width and mass of each plate were repeated $N_1 = 5$ times, whereas the measure of the thickness was acquired $N_2 = 10$ times for each plate. The values of length, width, thickness and mass reported in the table are the mean values of the repeated measurements.

6.2. Results and Discussion

In our application, the first guess for E_L , E_R and G_{LR} are obtained with Caldersmith's formulas. The remaining 6 material parameters of the first guess correspond to the nominal elastic constants of Red spruce published by Hearmon [19]. The minimization procedure of the *FRF2Params* method is run for $N_r = 10$ realizations.

We first compare the estimation of E_L , E_R and G_{LR} provided by the *FRF2Params* method with the estimations of the aforementioned parameters obtained with Caldersmith's formulas. Table 6.2 summarizes the values of E_L , E_R and G_{LR} fed as first guess to the *FRF2Params* method (i.e. obtained with Caldersmith's formulas) and the estimations provided by the method itself. We can see that the *FRF2Params* method yields slightly modified elastic constants, meaning that the estimation provided by Caldersmith is already around a local minimum of the loss function.

The correctness of the estimated material parameters is evaluated by comparing one another the measured point FRF and a simulated point FRF computed for the estimate of the material parameters provided by the *FRF2Params* method. Both point FRFs are evaluated in the frequency range $[0, 1200]$ Hz. The simulated point FRF is evaluated at the measurement points defined in Chapter 3 over a plate with the same geometry of the measured one.

Two different metrics are computed between the FRFs. One is the Frequency Response

sample	Material Parameters [GPa]					
	E_{LC}	E_{LF}	E_{RC}	E_{RF}	G_{LR_C}	G_{LR_F}
1_L	9.3	9.7	1.040	0.783	0.489	0.513
1_R	11.5	11.8	0.720	1.03	0.689	0.758
2_L	10.9	10.7	0.981	0.976	0.597	0.682
2_R	12.0	11.6	1.058	0.964	0.678	0.756
3_L	10.2	9.01	1.307	0.906	0.871	0.888
3_R	8.8	8.8	0.673	0.784	0.768	0.878
4_L	12.4	11.9	0.994	1.010	0.705	0.816
4_R	15.9	15.0	0.717	1.320	0.892	0.968
5_L	12.4	12.1	0.981	0.999	0.737	0.798
5_R	11.2	10.8	0.977	0.970	0.714	0.794

Table 6.2: Values of the estimation of E_L , E_R and G_{LR} provided both by Caldersmith's formulas (indicated with C subscript) and the *FRF2Params* method (indicated with F subscript).

Assurance Criterion (FRAC) [20], which provides a measure of the similarity between two FRFs. The FRAC is defined as

$$\text{FRAC}(H_A, H_B) = \frac{\left| \sum_{j=1}^{N_f} (H_A(f_j)^* H_B(f_j)) \right|^2}{\left[\sum_{j=1}^{N_f} (H_A(f_j)^* H_B(f_j)) \right] \left[\sum_{j=1}^{N_f} (H_A(f_j)^* H_B(f_j)) \right]}, \quad (6.3)$$

where H_A and H_B are two complex-valued frequency response functions, f is the frequency, N_f is the number of frequency bins in the frequency range of interest. The FRAC is a quite popular metric and has been widely employed to compare simulated and experimental FRFs [29]. It yields a value in the interval $[0, 1]$, where 1 is total similarity and 0 is no similarity. This metric is insensitive to constant differences, which is desirable for our case, since simulated and measured FRFs have different mean values (see the left part of Fig. 5.2 as an example).

The second metric we evaluate is the Normalised Mean Squared Error (NMSE) between the FRFs, expressed in dB . In order to avoid constant differences, before computing the NMSE we perform min-max normalization on both FRFs. The NMSE provides a measure of the mean relative error between two discrete series and it is computed as

$$\text{NMSE}(\hat{y}, y) = \frac{\|\hat{y} - y\|_2^2}{\|\hat{y}\|_2^2}, \quad (6.4)$$

where $\|\cdot\|_2$ is the \mathcal{L}_2 norm, \hat{y} is the actual value of a variable and y is its estimation. Optionally, the NMSE can be expressed in dB .

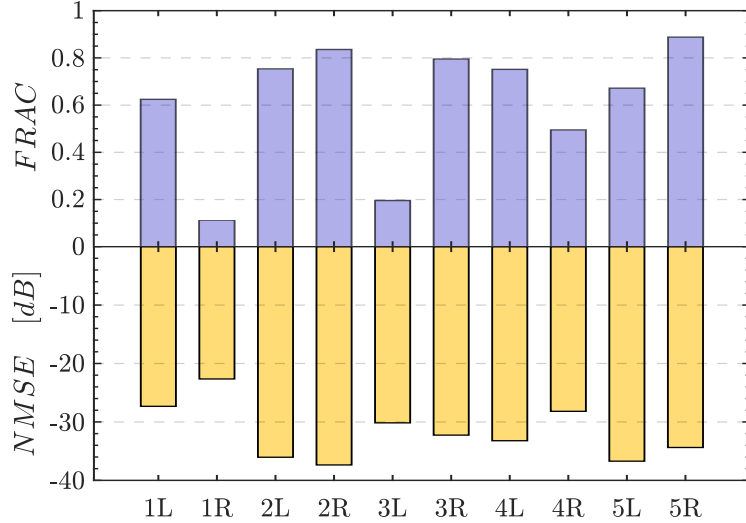


Figure 6.2: FRAC and NMSE between the experimental point FRFs of each plate and the simulated point FRFs computed for the material properties estimated by the *FRF2Params* method.

Figure 6.2 summarizes the results in terms of FRAC and NMSE between simulated and experimental FRFs. The NMSE is expressed in dB . The metrics are supposed to be evaluated together, as an high FRAC and a low NMSE indicate high similarity and a small point by point difference, respectively. The estimation of the material parameters for plates $2L/2R$ and $5L/5R$ are the best performing ones, whereas the estimations related to plates 1_R and 3_L are the worst performing ones. It is worth noticing that the plates belonging to pairs 2 and 5 are the most regular, with 2_R more regular than 2_L (see Fig. 6.1). On the other hand, plates 1_L , 1_R , 3_L and 4_R suffer from relevant geometry defects and their performance is characterized by a low FRAC and a high NMSE. This suggests that the regularity of the plate geometry is an important aspect and should not be underestimated.

Fig. 6.3 depicts the measured and the simulated FRF of plate 2_R . We can see that the ordering of the peaks of both simulated and measured FRFs coincide, indicating that the estimation of the material parameters is accurate. It is worth to mention that even though the *FRF2Params* method matches only the first 12 peaks of the measured FRF, the estimated FRF displays a very good level of agreement for all the peaks (i.e. 19 peaks) shown in the figure.

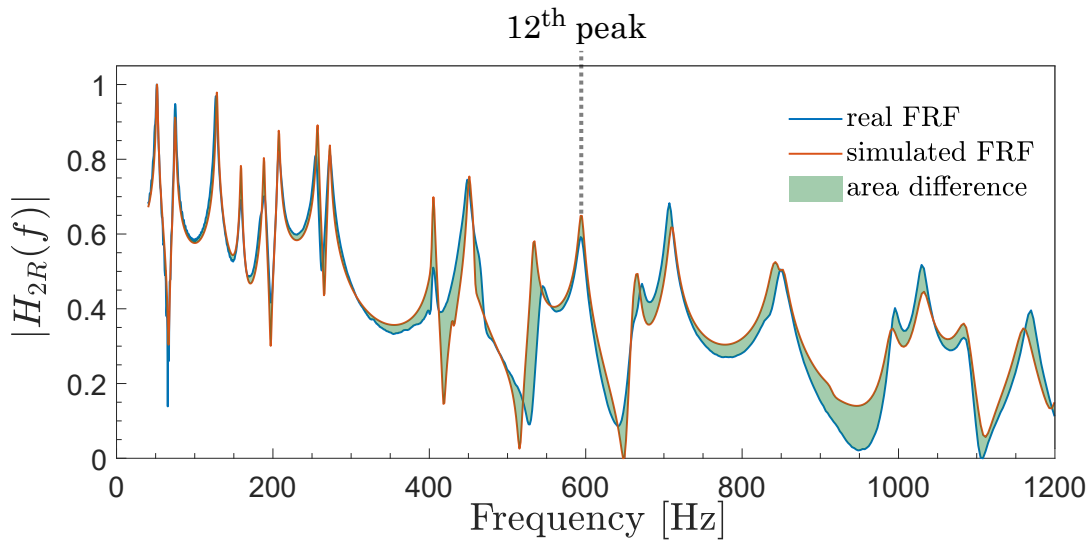


Figure 6.3: FRF of the plate 2_R and simulated FRF of a plate with the same geometry of 2_R and the material parameters identified with the *FRF2Params* method. It is clearly visible that the estimate of the material properties is very accurate, as all the modes depicted in the figure have the same order and the maximum relative error between corresponding peaks is below 5%.

6.3. Concluding Remarks

In this chapter we validate the *FRF2Params* method with a set of 10 classical guitar plates and discuss its results. First, the set plates is introduced and the measurements performed on each plate are illustrated. Secondly, the estimations of the material properties of the plates obtained with the *FRF2Params* are presented. The quality of the estimations is evaluated and related to the defects of the plates geometry. Overall, the *FRF2Params* proves to yield a satisfactory estimation of the material properties whenever the geometry of the plate is regular.

7

Conclusions And Future Work

7.1. Limitations and Future Works

7.2. Limitations

Albeit providing the simultaneous estimation of all the material parameters of the plate, the *FRF2Params* method suffers from some limitations. The most important limitations result from the employment of Rayleigh damping as damping model. The fact that the control variables of the damping model, α and β , are user-defined results in a not fully automatic technique. Indeed, the user should input adequate damping constants, which requires either a time consuming trial and error process or the knowledge of at least two modal damping ratios.

A possible solution to this issue could be provided by including relative amplitude differences in the loss function and by excluding α and β from the set of constant parameters. In this way it would be ideally possible to estimate their optimal value.

We already tried undergoing this path. The *FRF2Params* method works well with such modifications (being then fully automatic), but after $N_r = 10$ realizations of the minimization process performed on plate 2_R , the standard deviation of α and β (expressed in percentage with respect to the mean values) are $\sigma_\alpha \sim 35\%$ and $\sigma_{beta} \sim 50\%$. Such values are very high with respect to the standard deviation of the density (i.e. which is set to the 2.5% of the measured value), indicating that the estimate of the damping constants in the same plate may be highly variable, and thus not that accurate.

Moreover, for a value of β matching the damping of mid frequency peaks, Rayleigh damping easily results into over-damped higher frequency peaks, whereas for β matching the damping of higher frequency peaks we have the under-damping of the mid frequency peaks. This issue limits the frequency bandwidth in which the *FRF2Params* can be applied up to 800 [Hz]. The over-damping/under-damping issue and the high variability of α and β rise the question whether Rayleigh damping is a good model for simulating wood

damping features.

A study on the use of Rayleigh damping as damping model for synthesising the sound coming from different materials of variable geometry clearly states that "the Rayleigh damping model does not provide a good approximation for materials with heterogeneous micro-structures, such as wood" [45]. A probably more adequate model for modeling damping would be a viscoelastic model, which takes into account the anisotropy of wood. Nevertheless, a viscoelastic model requires 9 variables, while Rayleigh damping requires only 2 variables. We chose to employ Rayleigh damping for the sake of simplicity, but in the future the *FRF2Params* method should involve both a viscoelastic model and relative amplitude differences in the loss function to estimate the loss factors. It is worth to mention that the knowledge of the loss factors would allow us to evaluate some important acoustical parameters of the plate, such the acoustic conversion efficiency and the anisotropy ratio.

7.3. Future Works

The most urgent future work for *FRF2Params* is a proper evaluation of the error associated to the method. Indeed, as stated by Viala "Both direct and indirect methods deal with uncertainties in the evaluation (direct methods) or identification (indirect methods) of the parameters values" [55] and in this thesis we were not able to give a measurement of such error. The estimates given by the *FRF2Params* method should be compared to the ones provided by acknowledged methods, such as quasi-static tests, as was done by Viala [55]. Moreover, in order to avoid irregularities and defects in the geometry, the wooden plates should be cut to a set of predefined geometries.

Another possible future work for the *FRF2Params* method involves the application of the method over wooden bodies with different geometry. The *FRF2Params* method should successfully work with wooden bodies of arbitrary geometry as long as such bodies are thin. Indeed, since the frequency value of the eigenfrequencies of a body is in general proportional to its thickness (e.g. as indicated, for a plate, by Caldersmith's formulas ??), a thick body has too few natural frequencies in the operative range of the *FRF2Params* method. Luckily, the soundboards of stringed instruments such as violins or guitars are thin structures. Even if the parametrization of their geometry is more complex with respect to the one of a plate, it is possible to train neural networks to predict their modal behaviour [18]. Thus, it should be possible to apply the *FRF2Params* method to simultaneously estimate their material properties.

Another interesting future work is the prediction of a FRF in its entirety and not just its

peaks. In this case, the method should be completely repurposed. First, the FRF should be evaluated over a logarithmic axis of at least 150 points over the frequency range [0, 1000] Hz in order to have a clear representation of its peaks. Second, a feedforward neural network would probably not be suited for such a large number of outputs. A more complex and powerful neural network, such as a convolutional neural network, should be employed. At last, the loss function should be reformulated. A suitable loss function for this task should minimize the normalised mean squared error between estimated and measured FRFs and maximize their similarity.

The main advantage of this approach is that it would be surely more robust than *FRF2Params* method as it is now. Indeed, there would be no need to evaluate the distance between points and build a map of associations. On the other hand, the generation of a dataset containing the complete FRF would result to a much greater computation time with respect to the one of the G_{30} , where only 15 points are used. Moreover, the training of the neural network would probably take more time, and its design would be more complex.

7.4. Conclusions

This thesis presents a novel data-driven technique for the characterization of classical guitar plates. The technique is called *FRF2Params* method and allows to simultaneously estimate all the material parameters of a plate starting from a single frequency response function evaluated at prescribed points of its surface. In particular, the excitation and measuring points for which the FRF is evaluated are at 2 cm from the edges of opposite corners. Once the FRF is acquired, the method only requires the peaks of the measured FRF, without any need of further analysis.

The technique is based on a synthetic dataset that simulates the measurement of a point FRF evaluated at the aforementioned points. The dataset contains the frequency and the amplitude of the FRF peaks as the material parameters, the density and the geometry of the plate vary. The damping of the plate is modeled by means of Rayleigh damping. Two feedforward neural networks, one for frequency and another for amplitude, are trained on the dataset thus providing a fast prediction of the modal behaviour of the plate starting from its material properties, its density, its geometry and the control variables of the damping model. The final material properties are identified by means of a minimization procedure. The objective function of the minimization procedure is computed in the frequency/amplitude space and evaluates the frequency distance between the estimated FRF peaks and the measured ones. As a result, the outputs of the minimization procedure are the material properties that minimize the distance between such peaks.

The minimization process is repeated for $N_r = 10$ realizations. At each realization the density of the plate is associated to a gaussian random variable centered on the measured value of the density and with a standard deviation equal to the 2.5% of the mean. The final estimate of the mechanical parameters is given by the mean of the results given by $N_r = 10$ minimizations.

The use of neural networks allows to greatly accelerate the computation time associated to the estimation. Indeed, the inference time of a finite element solver is three order of magnitude higher than the inference time of a neural network. Since it provides a fast and accurate estimation of the material properties, this procedure may be seen as a first step towards a neural network-driven tool that can help guitar makers in the making of their instruments, starting from the choice of the tonewood. That is, this thesis work opens the door for guitar design based on an accurate knowledge of the material properties of a given wooden sample, which is still not done today.

We chose to develop the methodology for wooden plates because of their simple geometry and their wide employment in the musical acoustics field. Nevertheless, we wish to extend this approach to complex geometries, such as violin top-plates, guitar top-plates and piano soundboards. Moreover, in order to extend the frequency range of application of the *FRF2Params* method, in the future we will employ a more suitable damping model with respect to Rayleigh damping.

Bibliography

- [1] F. Aldakheel, R. Satari, and P. Wriggers. Feed-forward neural networks for failure mechanics problems. *Applied Sciences*, 11(14):64–83, 2021.
- [2] P. Ball. Violin makers can't pick out good wood. *Nature news*, 2007.
- [3] C. Barlow. Materials selection for musical instruments. *Proceedings institute of acoustics*, 19:69–78, 1997.
- [4] M. H. Beale, M. T. Hagan, and H. B. Demuth. Neural network toolbox users guide. *The MathWorks Inc*, 103, 1992.
- [5] J. Bodig and B. Jayne. *Mechanics of Wood and Composites*. Van Nostrand Reinhold Company, 1982.
- [6] A. Brauchler, P. Ziegler, and P. Eberhard. An entirely reverse-engineered finite element model of a classical guitar in comparison with experimental data. *The Journal of the Acoustical Society of America*, 149(6):4450–4462, 2021.
- [7] L. Bruno, G. Felice, L. Pagnotta, A. Poggialini, and G. Stigliano. Elastic characterization of orthotropic plates of any shape via static testing. *International Journal of Solids and Structures*, 45(3-4):908–920, 2008.
- [8] V. Bucur. *Handbook of Materials for String Musical Instruments*. Springer, 2016.
doi: 10.1007/978-3-319-32080-9.
- [9] C. Buksnowitz, A. Teischinger, U. Müller, A. Pahler, and R. Evans. Resonance wood [*picea abies* (l.) karst.]-evaluation and prediction of violin makers quality-grading. *The journal of the acoustical society of America*, 121(4):2384–2395, 2007.
- [10] G. Caldersmith. Vibrations of orthotropic rectangular plates. *Acta Acustica united with Acustica*, 56(2):144–152, 1984.
- [11] G. Caldersmith and F. Elizabeth. Wood properties from sample plate measurements i. *Journal of Catgut Acoustic*, 1(II):8–12, 1990.
- [12] C. Carlier, A. Alkadri, J. Gril, and I. Bremaud. Revisiting the notion of "resonance

- wood" choice: a decompartmentalised approach from violin makers' opinion and perception to characterization of material properties variability. wooden musical instruments. *Wooden musical instruments - Different forms of knowledge : Book of end of WoodMusICK COST Action FP1302*, pages 119–142, 2018.
- [13] N. R. Draper and H. Smith. *Applied regression analysis*, volume 326. John Wiley & Sons, 1998.
 - [14] N. H. Fletcher and T. D. Rossing. *The physics of musical instruments*. Springer Science & Business Media, 2012.
 - [15] E. Fouilhe, A. Houssay, and I. Brémaud. Dense and hard woods in musical instrument making : Comparison of mechanical properties and perceptual "quality" grading. 05 2012.
 - [16] S. Glantz and B. Slinker. *Primer of Applied Regression & Analysis of Variance*, ed. McGraw-Hill, Inc., New York, 2001.
 - [17] S. Gonzalez, D. Salvi, F. Antonacci, and A. Sarti. Eigenfrequency optimisation of free violin plates. *The Journal of the Acoustical Society of America*, 149(3):1400–1410, 2021.
 - [18] S. Gonzalez, D. Salvi, D. Baeza, F. Antonacci, and A. Sarti. A data-driven approach to violin making. *Scientific reports*, 11(1):1–9, 2021.
 - [19] R. F. S. Hearmon. The elasticity of wood and plywood. *Forest Products Research*, 1948.
 - [20] W. Heylen and S. Lammens. Frac: a consistent way of comparing frequency response functions. In *Proceedings of the conference on identification in engineering systems*, pages 48–57, 1996.
 - [21] K. Hornik, M. Stinchcombe, and H. White. Multilayer feedforward networks are universal approximators. *Neural networks*, 2(5):359–366, 1989.
 - [22] E. H. Idrobo-Ávila and R. Vargas. Acoustic and mechanic characterization of materials used in manufacturing the soundboard of the spanish guitar: Influence in the sonority. *Revista Facultad de Ingeniería Universidad de Antioquia*, 2015, 12 2015. doi: 10.17533/udea.redin.n76a04.
 - [23] F. P. R. Institute. *Wood Industry Handbook*. Mamzen Company Ltd.
 - [24] H. H. Ku. Notes on the use of propagation of error formulas. *Journal of Research of the National Bureau of Standards*, 70(4):263–273, 1966.

- [25] F. P. Laboratory. *Wood Handbook*. US. Department of Agriculture, 1974.
- [26] J. C. Lagarias, J. A. Reeds, M. H. Wright, and P. E. Wright. Convergence properties of the nelder-mead simplex method in low dimensions. *SIAM Journal on optimization*, 9(1):112–147, 1998.
- [27] D. Larsson. Using modal analysis for estimation of anisotropic material constants. *Journal of Engineering Mechanics-asce*, 123:222–229, 1997.
- [28] T. Lauwagie, H. Sol, W. Heylen, and G. Roebben. Determination of the in-plane elastic properties of the different layers of laminated plates by means of vibration testing and model updating. *Journal of Sound and Vibration*, 274(3-5):529–546, 2004.
- [29] D. Lee, T. Ahn, and H. S. Kim. A metric on the similarity between two frequency response functions. *Journal of Sound and Vibration*, 436:32–45, 2018.
- [30] M. McIntrye and J. Woodhouse. On measuring wood properties, part 1. *Journal Catgut Acoustical Society*, 42:11–15, 1984.
- [31] M. McIntrye and J. Woodhouse. On measuring wood properties, part 2. *Journal Catgut Acoustical Society*, 43:18–24, 1985.
- [32] M. McIntrye and J. Woodhouse. On measuring wood properties, part 3. *Journal Catgut Acoustical Society*, 45:14–23, 1986.
- [33] L. Mehrez, A. Doostan, D. Moens, and D. Vandepitte. Stochastic identification of composite material properties from limited experimental databases, part ii: Uncertainty modelling. *Mechanical Systems and Signal Processing*, 27:484–498, 2012.
- [34] L. Mehrez, D. Moens, and D. Vandepitte. Stochastic identification of composite material properties from limited experimental databases, part i: Experimental database construction. *Mechanical Systems and Signal Processing*, 27:471–483, 2012.
- [35] L. Meirovitch. *Fundamentals of Vibrations, Long Grove*. Waveland Press, 2001.
- [36] N. Molin, T. Tinnsten, U. Wiklund, and E. V. Jansson. Fem-analysis of an orthotropic shell to determine material parameters of wood and vibration modes of violin plates. *STL-QPSR*, 25(56):11–37, 1984.
- [37] J. J. Moré. The levenberg-marquardt algorithm: implementation and theory. In *Numerical analysis*, pages 105–116. Springer, 1978.
- [38] E. Obataya, T. Ono, and M. Norimoto. Vibrational properties of wood along the grain. *Journal of Materials Science*, 35(12):2993–3001, 2000.

- [39] T. Ono and M. Norimoto. On physical criteria for the selection of wood for soundboards of musical instruments. *Rheologica acta*, 23(6):652–656, 1984.
- [40] P. Persson, O. Flodén, H. Danielsson, A. Peplow, and L. V. Andersen. Improved low-frequency performance of cross-laminated timber floor panels by informed material selection. *Applied Acoustics*, 179:108017, 2021.
- [41] L. Prechelt. Automatic early stopping using cross validation: quantifying the criteria. *Neural Networks*, 11(4):761–767, 1998.
- [42] W. H. Press, W. T. Vetterling, S. A. Teukolsky, and B. P. Flannery. *Numerical recipes*, volume 818. Cambridge university press Cambridge, 1986.
- [43] J. D. Pulfer and C. Waine. An efficient monte carlo approach to optimization. *Journal of chemical information and computer sciences*, 38(5):791–797, 1998.
- [44] J. Rayleigh. *The Theory of Sound, Volume One*. Dover Books on Physics. Dover Publications, 2013.
- [45] Z. Ren, H. Yeh, R. Klatzky, and M. C. Lin. Auditory perception of geometry-invariant material properties. *IEEE Transactions on Visualization and Computer Graphics*, 19(4):557–566, 2013.
- [46] M. H. Richardson. Structural dynamics measurements. *SD2000*, pages 1–13, 1999.
- [47] R. J. Ross et al. *Wood handbook: Wood as an engineering material*. The Laboratory, 2010.
- [48] J. C. Schelleng. The violin as a circuit. *The Journal of the Acoustical Society of America*, 35(3):326–338, 1963.
- [49] N. Sobue and M. Kitazumi. Identification of power spectrum peaks of vibrating completely-free wood plates and moduli of elasticity measurements. *Mokuzai Gakkaishi*, (37):9–15, 1991.
- [50] H. Sol, J. De Visscher, and W. De Wilde. Identification of the viscoelastic material properties of orthotropic plates using a mixed numerical/experimental technique. *WIT Transactions on Modelling and Simulation*, 5, 1993.
- [51] D. Svozil, V. Kvasnicka, and J. Pospichal. Introduction to multi-layer feed-forward neural networks. *Chemometrics and intelligent laboratory systems*, 39(1):43–62, 1997.
- [52] Y. Taniguchi, K. Ando, and H. Yamamoto. Determination of three-dimensional viscoelastic compliance in wood by tensile creep test. *Journal of Wood Science - J WOOD SCI*, 56:82–84, 2010. doi: 10.1007/s10086-009-1069-6.

- [53] A. Tolbecque. *L'art du luthier*. Editorial MAXTOR, 2013.
- [54] R. Viala. *Towards a model-based decision support tool for stringed musical instruments making*. PhD thesis, Bourgogne Franche-Comté, 2018.
- [55] R. Viala, V. Placet, and S. Cogan. Identification of the anisotropic elastic and damping properties of complex shape composite parts using an inverse method based on finite element model updating and 3d velocity fields measurements (femu-3dvf): Application to bio-based composite violin soundboards. *Composites Part A: Applied Science and Manufacturing*, 106:91–103, 2018.
- [56] R. Viala, V. Placet, and S. Cogan. Simultaneous non-destructive identification of multiple elastic and damping properties of spruce tonewood to improve grading. *Journal of Cultural Heritage*, 42:108–116, 2020.
- [57] U. G. Wegst. Wood for sound. *American Journal of Botany*, 93(10):1439–1448, 2006.
- [58] B. Yankovskii. Dissimilarity of the acoustic parameters of unseasoned and aged wood. *Soviet Physics, Acoustics*, 13:125–127, 1967.
- [59] H. Yano and H. Matsuhisa. Study on the timber of wood ii, analysis of the sound spectrum of wood using viscoelastic timoshenko equation. *Scientific Reports Kyoto Prefectural University*, 43:24–31, 1991.
- [60] S. Yoshikawa. Acoustical classification of woods for string instruments. *The Journal of the Acoustical Society of America*, 122(1):568–573, 2007.
- [61] J. Zhou, Y. H. Chui, M. Gong, and L. Hu. Comparative study on measurement of elastic constants of wood-based panels using modal testing: choice of boundary conditions and calculation methods. *Journal of Wood Science*, 63(5):523–538, 2017.
- [62] O. C. Zienkiewicz, R. L. Taylor, P. Nithiarasu, and J. Zhu. *The finite element method*, volume 3. McGraw-Hill London, 1977.

List of Figures

1.1	Chladni patterns of the modal shapes employed for the estimation of the material parameters of the plate with Caldersmith's formulas (Caldersmith & Freeman, 1990, p. 9 [11])	2
1.2	Complete pipeline of the <i>FRF2Params</i> method.	5
2.1	Application of an axial load F_1 and a shear load F_2 , considering the surface A_1 . $\sigma_{11} = F_1/A_1$ is the axial stress along the x_1 direction, while $\sigma_{12} = F_2/A_1$ is the shear stress along the x_1 and x_2 directions. When loading the body over the surface A, a reacting force of equal magnitude and opposite verse will appear on the opposite surface due to the third principle of dynamics.	8
2.2	Principal axes of the wood. The direction of the grains is indicated by the blue arrow while the growth rings are pointed out by the green arrow. The longitudinal axis is parallel to the grains and the growth rings, the tangential axis is tangent to the growth rings and normal to the grains and the radial axis is normal both to the grains and the growth rings. Wood has different and independent mechanical properties along the three axes.	11
2.3	Example of magnitude (up) and phase (down) of a frequency response function. In particular, the FRF depicted in the figure is a receptance (i.e. displacement/force). We can see four resonances and one antiresonance, which are highlighted by four red circles and a green square, respectively. Each resonance corresponds to a local maximum in the magnitude plot and a decrease of 180° in the phase plot, whereas the antiresonance is associated to a local minimum in the magnitude plot and an increase of 180° in the phase plot.	18
2.4	Modal damping ratio resulting from the Rayleigh damping model with $\alpha = 5[s]$ and $\beta = 5 \times 10^{-6}$. It can be seen that the resulting modal damping ratios mainly depend from α for lower frequency modes, whereas they mainly depend from β for higher frequency modes.	22

2.5 Example of point Frequency Response Function (FRF) of a wooden thin plate. The modes depicted in the figure are from left to right: (1, 1), (0, 2), (1, 2), (2, 0), (2, 1), (2, 2). The amplitude associated to each eigenfrequency is proportional to the product of the modal shape evaluated at the excitation and measuring points, that are depicted in white on each modal shape.	24
2.6 Characteristic modes of a wooden thin plate. From left to right we can see mode (0, 2), mode (2, 0) and mode (1, 1), which are the fundamental longitudinal bending mode, the fundamental radial bending mode and the fundamental twisting mode, respectively. The first is related to the longitudinal Young modulus E_L , the second to the radial Young modulus E_R and the third to the longitudinal to radial shear modulus G_{LR}	25
3.1 Guitar plates glued together to build a guitar soundboard. The geometry of a single guitar plate is standardized to $(580 \times 215 \times 4)$ mm. Small geometry variations are allowed. The wood grain direction is oriented along the longitudinal direction of the plate.	30
3.2 Normalized sum between the absolute value of the modal shapes relative to the first $S = 15$ eigenfrequencies obtained with the nominal material parameters of Red spruce and the standard geometry of classical guitar plates. The overall displacement field is maximum around the corners of the plate.	31
3.3 Schematic of the modeled guitar plates. The length, the width and the thickness of the plates vary throughout the dataset. The excitation and measurement points are depicted in blue and red, respectively. The points are placed at opposite corners of the plate at 20mm from the edges.	32
3.4 First three modal shapes of a Poisson plate, which is a plate that satisfies Eq. 3.4. The modal shapes of a poisson plate have fixed geometry and fixed order of appearance along the frequency axis. We can see, from left to right, the "cross" mode, the "x" or "saddle" mode and the "circle" or "breathing" mode.	34
3.5 First 15 modal shapes of the reference set, which is obtained for the nominal parameters of the dataset (see Table 3.1).	35
3.6 Left: distribution in frequency of the first six peaks in ascending order. Right: distribution in frequency of the first six modes after modal shapes identification (right).	37

3.7 Pearson correlation coefficients between the eigenfrequencies and the density, the elastic constants E_L , E_R , G_{LR} and the geometry parameters. Left : dataset sorted by peaks. Right : dataset sorted by modes.	38
4.1 Diagram of a multilayer feedforward neural network. The neural network depicted in the figure has two inputs in the input layer x , two outputs in the output layer \hat{y} and \mathcal{L}_n hidden layers of five neurons each. The total number of layers and the number of neurons per layer define the topology of the neural network. In particular, the neural network depicted above is a $(5 \times \mathcal{L}_n)$ MFNN.	42
4.2 Hyperparameters tuning of the network trained with the G_{30} dataset. The matrices show the $\overline{R^2}$ defined in eq. (4.1) computed on the test set, obtained by randomly sampling the 10% of the occurrences of the G_{30}	43
4.3 Left : train, test and validation losses versus the epoch number for a 64×4 MFNN trained with the G_{30} dataset. The model is too complex for the training data. As a result, overfitting is not avoided and the mean squared error on the validation set (i.e. the best validation performance) is high. Right : train, test and validation losses versus the epoch number for a (16×2) MFNN. The expressivity of the model meets the complexity of the training data. Therefore the discrepancy between the losses stays acceptable until the plateau is reached and the early stopping criteria are triggered, thus avoiding overfitting.	44
4.4 Results of the study performed to test the generalization of the MFNNs. Both neural networks are tested with four uniformly distributed U_s test sets. The U_s test sets are characterized by an increasing span of the distributions associated to the material parameters and the density, namely set to the 25%, 50%, 75% and 95% of the nominal values. The figure shows the mean coefficient of determination $\overline{R^2}$ (see eq. (4.1)) relative to the prediction of frequency and amplitude versus the span of the test set.	45
5.1 Iterative pipeline of a minimization procedure. The minimization runs on the multidimensional space defined by the material parameters only (i.e. 9 parameters). During the minimization the density ρ , the geometry parameters l , w and h and the control variables of Rayleigh damping α and β are fixed.	49

5.2 Normalization between estimated FRF peaks and measured FRF peaks. Left: measured FRF peaks and estimated FRF peaks without any modification. Left: resulting peaks after the normalization (see Eqs. (5.2) and (5.1)).	50
5.3 Evolution of the loss function for a single minimization task. In the left part of the figure we can see the <i>estimated peaks</i> and <i>measured peaks</i> corresponding to the first guess of the material parameters, while in the right part we can see how the frequency/amplitude pairs are distributed at the end of the minimization. The black lines connect each <i>measured peak</i> to the closest <i>estimated peak</i>	52
6.1 Set of 10 classical guitar plates made of Red spruce that we measured and characterize. We can see that most of the plates exhibit an irregular geometry, in particular: (i) the pairs $1_L/1_R$ and $4_L/4_R$ display relevant irregularities at their corners; (ii) the pair $3_L/3_R$ shows moderate imperfections (3_L has irregular edges, while 3_R does not); (iii) the pairs $2_L/2_R$ and $5_L/5_R$ have either no defects or neglectable defects.	56
6.2 FRAC and NMSE between the experimental point FRFs of each plate and the simulated point FRFs computed for the material properties estimated by the <i>FRF2Params</i> method.	59
6.3 FRF of the plate 2_R and simulated FRF of a plate with the same geometry of 2_R and the material parameters identified with the <i>FRF2Params</i> method. It is clearly visible that the estimate of the material properties is very accurate, as all the modes depicted in the figure have the same order and the maximum relative error between corresponding peaks is below 5%.	60

List of Tables

2.1	Different types of FRF. Depending on the physical quantity used to evaluate the motion of the body, the FRF can be categorized either as a receptance, a mobility or an inertance.	16
3.1	Mean values of the material and geometry parameters of the dataset. E_{L_0} , E_{R_0} and G_{LR_0} are the average values of the E_L , E_R and G_{LR} obtained with Caldersmith's formulas on our set of 10 classical guitar plates. The rest of the material parameters are the nominal elastic constants of Red spruce published by Hearmon [19].	33
3.2	Standard deviations associated to density, material parameters and geometry parameters.	33
3.3	Associations between the first six modes of the dataset and the first six peaks of the FRF in ascending order.	38
5.1	Comparison between the computation time associated to the calculations of the finite element model of the plate and the inference time of the neural network, both for frequency and amplitude. The third column of the table expresses the speed gain defined in Eq. (5.9).	54
6.1	Measured values of the geometry and density of each plate along with the uncertainty associated to the measurement of the density. The measurements of length, width and mass of each plate were repeated $N_1 = 5$ times, whereas the measure of the thickness was acquired $N_2 = 10$ times for each plate. The values of length, width, thickness and mass reported in the table are the mean values of the repeated measurements.	57
6.2	Values of the estimation of E_L , E_R and G_{LR} provided both by Caldersmith's formulas (indicated with C subscript) and the <i>FRF2Params</i> method (indicated with F subscript).	58

List of Symbols

Variable	Description	SI unit
u	displacement	m
σ_{ij}	stress	Nm ⁻²
ε_{ij}	strain	~
\mathcal{F}	force	N
A	area	m ²
E	Young's modulus	Pa
G	Shear modulus	Pa
C_{ij}	entry of the stiffness matrix	Pa
ν	Poisson's ratio	~
L	longitudinal direction	~
R	radial direction	~
T	tangential direction	~
E_L	longitudinal Young's modulus	Pa
E_R	radial Young's modulus	Pa
E_T	tangential Young's modulus	Pa
G_{LR}	longitudinal to radial Shear modulus	Pa
G_{RT}	radial to tangential Shear modulus	Pa
G_{LT}	longitudinal to tangential Shear modulus	Pa
ν_{LR}	longitudinal to radial Poisson's ratio	~
ν_{RT}	radial to tangential Poisson's ratio	~
ν_{LT}	longitudinal to tangential Poisson's ratio	~
ρ	density	kgm ⁻³
ω	radians frequency	rad s ⁻¹
X	spectrum of the displacement	m
\mathcal{F}	spectrum of the force	N

xi_i	modal damping ratio of the i^{th} mode	\sim
ω_i	i^{th} natural frequency	rad s^{-1}
f_i	i^{th} natural frequency	Hz
Φ	modal shape of a body	m
α	mass Rayleigh damping constant	s
β	stiffness Rayleigh damping constant	s
m	first mode number of a plate	\sim
n	second mode number of a plate	\sim
(m, n)	modal shape of a plate	\sim
$f_{(m, n)}$	eigenfrequency of a plate	Hz
l	length	m
w	width	m
h	thickness	m
Y	input parameter of the dataset	various
Y_0	center value of an input parameter	various
δ_Y	Gaussian random variable associated to an input parameter	\sim
$\hat{\sigma}$	standard deviation of the input parameters	\sim
σ	standard deviation of a Gaussian random variable or of a measurement	\sim
$U(a, b)$	uniform random variable	\sim
f_I, f_{II}, \dots	eigenfrequencies in their order of appearance (peaks)	Hz
\mathcal{L}	number of layers of a feedforward neural network	\sim
\mathcal{M}	number of neurons per layer of a feedforward neural network	\sim
R^2	coefficient of determination	\sim
\bar{R}^2	mean coefficient of determination	\sim
R	number of peaks of the measured FRF used in the <i>FRF2Params</i> method	\sim
S	number of eigenfrequencies of the dataset	\sim
f_s	frequency of the s^{th} estimated FRF peak	Hz
\hat{f}_r	frequency of the r^{th} peak of the measured FRF	Hz
a_s	amplitude of the s^{th} estimated FRF peak (in dB)	\sim
\hat{a}_r	amplitude of the r^{th} peak of the measured FRF (in dB)	\sim
\hat{L}_2	objective function of the minimization	\sim
t_P	inference time of a predictor	s
t_{FE}	computation time of a finite element model	s

G_P	speed gain between predictor and finite element model	\sim
v	volume of a plate	m^3
M	mass of a plate	kg

Acknowledgements

My sincere and deep thanks go to Professor Fabio Antonacci. I thank him not only for his help and his constant support during the production of this thesis, but also for sharing his passion for musical instruments and musical acoustics with me.

I would also like to recognize the invaluable guidance of my supervisors Sebastian Gonzalez and Raffaele Malvermi and thank them for their patience, their constant support and their keen feedback. They made me grow and overcome some of my limits, I am very grateful to them.

My thoughts go also to my mates of adventures in Cremona, my colleagues Miriam, Alessio and Mattia. This journey would have not been this nice if you were not there.

Last but not least, I am grateful to my family for their continuous and unconditional support. I dedicate this thesis to my uncle, Lelio Giannetto.

